An experimental setup with radial injection cell for investigation of fracturing in unconsolidated sand reservoirs under fluid injection

Thanh Tung Nguyen, Jean Sulem, Rawaz Dlawar Muhammed, Jean-Claude Dupla, Jean Canou, Jean-Grégoire Boero-Rollo, Jalel Ochi

An experimental setup with radial injection cell for investigation of fracturing in unconsolidated sand reservoirs under fluid injection

Thanh Tung Nguyen[(1)], Jean Sulem[(1)], Rawaz Dlawar Muhammed[(1)], Jean-Claude Dupla[(1)], Jean Canou[(1)], Jean-Grégoire Boero-Rollo[(2)], Jalel Ochi[(2)]

(1) Laboratoire Navier, Ecole des Ponts ParisTech, Univ. Gustave Eiffel, CNRS, Marne-la-Vallée, France

(2) TotalEnergies, Pau, France

Highlights

- A new experimental device is developed for studying hydraulic fracturing of dense sand specimens.
- Fractures are not tensile cracks but appear as localized zones of higher porosity and larger pore size resulting from dilatant shearing and fine particles transport.
- Higher flow rate enhances fine particles transport which results in the extension and the opening of the pseudo-fractures.
- The fracturing pressure is controlled by the confining pressure and does not change significantly with the stress ratio and with the initial permeability of the sand specimen.

Abstract

Formation damage and the associated injectivity loss of wells induced by the produced water re-injection can be often overcome by injecting in the fracturing injection regime. This paper presents an experimental investigation of fracturing mechanisms induced in unconsolidated sand reservoirs under fluid injection using a new radial injection setup. The development of the injection cell is based on a radial injection configuration within a classical triaxial cell to simulate the injection wells conditions and this cell allows the whole specimen to be scanned using X-ray Computed Tomography (X-ray CT). Typical test results exhibit pressure drops during fluid injection corresponding to fracturing of the specimen, and consequently to an increase of the overall permeability. This can be confirmed by the detection of small radial fractures (‘pseudo-cracks’) around the injection point either by visual observation when disassembling the specimen or by 3D X-ray CT. Fractures appear as localized zones of higher porosity and larger pore size resulting from dilatant shearing and subsequent particles transport. The impact of various parameters (confining pressure, stress ratio coefficient, flow rate, permeability) on the fracturing process in sand specimens is explored. The obtained experimental results suggest that confining pressure is a key parameter controlling fracture initiation.

Keywords: Radial injection cell, Fracturing flow regime, Fracturing mechanisms, PWRI, Unconsolidated sand reservoirs, X-ray Computed Tomography.

1. Introduction

In hydrocarbon producing fields, Produced Water Re-Injection (PWRI) is known as an economically attractive and environmentally friendly method for managing produced water. This method has the advantage of pressure maintenance support and sweeping efficiency in order to enhance the hydrocarbon production (Farajzadeh, 2004; Souilah et al., 2014). However, despite many treatment processes, there is always a small amount of impurities, such as suspended solid particles of several microns and oil droplets in the injected water (Mainguy et al., 2020). Once the produced water is re-injected into reservoirs, the filtration of these components around the injection well leads to progressive clogging of the medium, and consequently, to the decline of the injectivity (Al-Abduwani et al., 2005; Li and Wong, 2008; Feia et al., 2015, 2017). The formation of filter cakes, due to the deposited solid particles in the near-wellbore region, is viewed as the dominant mechanism of the formation damage (i.e. permeability decrease) during PWRI (Shutong and Sharma, 1997). This issue is of particular importance for unconsolidated sand reservoirs. Although the formation has a high initial porosity and a high permeability (of the order of few Darcy), transport and deposition of suspended particles carried by the produced water deteriorate the well injectivity. Once formation damage occurs, several treatments can be applied for improving well injectivity in the matrix flow regime such as clean water injection (to flush away a fraction of deposited particles in the near-wellbore region) or chemical additives injection (to destabilize the filter cake and to clean the sand controls screen) (Souilah et al., 2014; Mainguy et al., 2020). Using these techniques may partially restore the injectivity loss but the beneficial effect disappears soon after PWRI resumes and these techniques require a substantial cost compared to the benefits they bring. On the other hand, re-injection in the so-called ‘fracturing regime’ is an option to maintain the injectivity by fracturing the clogged zone formed by the agglomeration of fine particles at the face of the injected formation (Ochi et al., 2014; Mainguy et al., 2020). However, controlling the injection in the fracturing regime is a key issue for the safety of the production as possible loss of fractures containment could deteriorate the cap rock integrity (Onaisi et al., 2011).

Hydraulic fracturing is commonly applied in consolidated rock reservoirs for enhancing oil and gas production. The first experimental fracturing was conducted in the Hogoton field in 1947 (Montgomery et al., 2010) Since that time, hydraulic fracturing has been one of the primary engineering tools for enhancing oil recovery. It is estimated that more than 90% of gas wells and 70% of oil wells throughout the world apply this technique (Economides and al., 2007). In the case of consolidated and brittle formations (e.g. hard rocks) with low permeability, hydraulic fracturing has been extensively studied (Detournay, 2016). Fracturing is dominated by tensile failure and conventional modeling is based on Linear Elastic Fracture Mechanics (LEFM) (Fjaer et al., 2008). Fracturing of soft rock formations, on the other hand, results in a higher net fluid pressure, shorter and wider fractures as compared to those obtained in a strong elastic formation because of the development of plastic zones at the fracture tip during fracture propagation and fluid leak off in the porous rock (Papanastasiou, 1997, 1999; Sarris and Papanastasiou, 2013). However, the dominant mechanism of fracturing in soft rocks is also tensile failure and fracture propagation is controlled by the rock toughness.

The mechanisms involved in fracturing of unconsolidated sand reservoirs, which are studied in the present work, are fundamentally different than the ones involved in brittle fracturing. Due to the negligible tensile strength as well as the extremely large fluid leak-off, the possibility of tensile failure is suppressed in favor of shear failure (Bohloli and de Pater, 2006; Zhai and Sharma, 2005), fluidization (Chang, 2004; Wu, 2006) or flow-induced channelization around an injection point (Ameen and Taleghani, 2015; Bautista and Taleghani, 2018; Mahadevan et al., 2012). During the last two decades,

several experimental studies have been dedicated to investigate the mechanisms and develop appropriate modeling of hydraulic fracturing in unconsolidated or poorly consolidated materials. However, the exact mechanisms involved in the fracturing process still remain an open issue. Khodaverdian and McElfresh, 2000 have performed a series of hydraulic fracturing experiments in a radial flow cell (RFC), which is a haft-cylinder (3-ft of radius). However, injection was performed through a rigid tube containing only some open holes that could not provide a radial configuration.

Bohloli and de Pater (2006); de Pater and Dong (2007); (2009); Dong (2010); Zhou et al. (2010) have conducted different experimental programs in axisymmetric cell to investigate the hydraulic fracturing for cohesionless soils. Different configurations of injection tube have been used such as the porous tube, the slotted open hole, open-hole interval, depending on the purpose of the research. Dong (2010) has used a similar axisymmetric cell (CT cell) with a smaller specimen size, allowing to visualize the fracture geometry in real-time by X-ray CT scanning. The CT cell is made of aluminum, which is able to apply a high confining pressure up to 20 MPa and is still X-ray transparent. However, as the image resolution of the CT scanner used in their study is rather limited as the smallest voxel size is of 300 μm, which is larger than sand grains size. Therefore, only large open fractures could be observed. An interesting work on hydraulic fracturing in cohesionless sand has been conducted by Golovin et al., (2010), (2011); Jasarevic et al. (2010); Chudnovsky et al. (2015); Wong et al. (2017). These authors have developed a special device for conducting hydraulic fracturing under 3D stress conditions. A cubic chamber with a dimension of 2ft (≈ 61 cm) for each edge is used. Nevertheless, the fluid was injected only through two opposing perforations (2 mm diameter) that provided a localized flow in the specimen which cannot simulate the radial flow conditions of PWRI as performed in the field. Another interesting study on hydraulic fracturing in particulate materials has performed by Chang (2004); Wu (2006); Germanovich et al. (2012); Hurt (2012).

Most of the studies mentioned above refers to frac-packing treatment or polymer flooding since they have been performed with very viscous fluids or with fluids containing a high concentration of solid particles with a high flow rate in order to enhance fracturing of the unconsolidated sand. Very few studies focus on the fracturing in the situation of PWRI in which the injected fluid has a very low viscosity (of the order 1 cP) and a low concentration of solid particles and in which the injection is maintained over a long period of time (Onaisi et al., 2011). In the present work, we aim at reproducing more realistic injection conditions by developing a new radial injection setup which permits to generate a radial flow through a cylindrical sand specimen under axial and radial confining stresses. The main objective of this work is to study the conditions for reaching the frac-regime and explore the fracturing mechanisms induced by the radial water injection in sand specimens containing particles which represents the clogged zone around the injection well due to PWRI. The experimental device and the experimental results are described in the following together with the observation of the fractured specimen using X-ray Computed Tomography (X-ray CT) and optical microscopy.

2. Experimental setup

A radial injection cell has been specially designed and built to study fracturing mechanisms in unconsolidated sand specimens under fluid injection. The main innovation in this new experimental setup is that it permits small scale observations using CT scanner. Thanks to a high resolution of X-ray CT in our laboratory, we could achieve a resolution of 29 μm per voxel. Specimens contain grains with a mean grain size D_{50} of 210 microns and fine particles of 20 microns. Therefore, it is possible to observe the microstructure of the specimen at the grain scale. Note that, for example, this resolution is 10 times higher than the one used in the work of Dong (2010). Another important feature of the experimental

device is the possibility to mimic the real injection process in the field by imposing a radial flow in the specimen by using a central injection tube. This tube contains open holes drilled in a helical groove. A lateral drainage system is installed around the specimen. This system permits to generate a radial flow which is homogeneous along and around the tube.

Fig. 1 shows a schematic cross section of radial injection cell with some of its major components. A cylindrical sand specimen of 100 mm in diameter and 200 mm in height with a controlled prescribed density can be built in the cell which is basically a classical triaxial cell with independent application of a confining stress and of an axial stress. In order to avoid the absorption of X-ray and metal artifact during scanning, the cell is fabricated with a limited number of metal pieces and can be easily transported. In particular, the scanned part (red rectangular in **Fig. 1**) is made of polymethyl methacrylate (PMMA) to facilitate the penetration of X-ray.

The cell consists of the following major components: an upper baseplate, a lower baseplate, a central tube attached to the lower baseplate, a peripheral drainage system, a lateral latex membrane and a confinement chamber. The upper and lower baseplates both consist of two separated pieces: one in PMMA and another in aluminum. Two rubber O-rings are positioned between the two pieces for sealing. The drainage system consists of two polyamide fabric sieves of cylindrical shape with an opening mesh of 80 µm, which allow for the retention of sand grains and for the passage of fine particles. The rubber O-rings are glued between these two sieves for maintaining a sufficient space for drainage and flow out of the fluid. **Fig. 2** shows a 3D schematic cross-section of the upper part of the cell with the drainage system for the fluid flow within the cell. On the upper baseplate, there are one outlet of the injection tube and two outlets of the lateral drainage system. Six small holes of 2 mm in diameter, drilled symmetrically inside the PMMA piece, allow to link the lateral drainage system with two outlets of the upper baseplate. The configuration of the central tube, made in PMMA, is presented in **Fig. 3**a. The inner and outer diameter of the central tube are 4 mm and 10 mm, respectively. Open holes are perforated on the helical groove, allowing to provide a radial fluid flow along the tube. The injection tube is covered by a 80 µm sieve to prevent the inflow of sand into the injection tube (**Fig. 3**b).

Fig. 4 and **Fig. 5** present a functional scheme and a general view of the experimental setup respectively. Injection was carried out with a G03 Hydra-Cell Pump at a constant flow rate with a range between 0.1 l/min and 2 l/min. A pulsation dampener, installed at the outlet of the pump, is used to reduce the pressure fluctuations and flow pulsations during injection. The injection rate is measured with a flowmeter installed at the inlet of the specimen. Three pressure transducers permit to monitor the confining pressure and the injection pressure at the inlet and at the outlet of the specimen. The accuracy of these sensors is of 0.5 kPa. The vertical stress is applied to the specimen through a 50 kN mechanical press Tri-SCAN. The axial force is measured using a force transducer installed on the top of the cell. The maximum capacity of the sensor is 10 kN with a measure accuracy of 0.004 kN. The confining pressure is applied using an air-water pressurization cell which has a maximum capacity of 1 MPa. All the measurement systems are connected to a computer through a multi-meter, allowing for automatic data acquisition and display of data in real time during the test. The acquisition frequency is manually set to one data point per 3 seconds.

3. Materials

In order to represent the clogged area around injection wells due to PWRI, the specimens of dense mixture of sand and fine particles are reconstituted by compaction. Fontainebleau NE34 sand and C10 silica particles are used. Fontainebleau sand has sub-rounded grains (D_{50} = 210 μm for NE34) and is composed of 99% silica. C10 is also composed of silica particles (D_{50} = 20 μm), allowing to avoid any chemical interaction with NE34 sand. Its physical properties are similar to those of NE34 sand. The main characteristics of these materials are presented in **Table 1**. **Fig. 6** presents the grain size distribution of both materials obtained from laser diffraction analysis. The preparation of the mixture of NE34 sand and C10 particles is carried out using a mixer and its homogeneity is validated by analyzing samples containing different concentrations of C10 particles (10% and 20%) using laser granulometer. The particles concentration is defined as the percentage in mass of C10 particles to NE34 sand (m_{C10} / m_{NE34}). As can be seen in **Fig. 6**,a good consistency in terms of the grain size distribution of the mixture is observed. Microscopic views of pure NE34 sand and of NE34 sand mixed with 22% of C10 particles are presented in **Fig. 6**b,c.

In the experiments, a colloidal silica is used to solidify the specimen after fracturing. It is a stable aqueous suspension (colloid) of nanometric silica particles. The particles size is between 7 and 22 nm (Gallagher and Lin, 2009). The nanosilica suspension can be gelled by raising the pH or changing ionic strength of the solution. The gel time depends on the interaction rate between particles, which is influenced by many factors such as the silica particle size, the ionic strength, the pH, and the temperature (Persoff et al., 1999).

The colloidal silica used in this research is commercially referenced as MasterRoc MP320. It was provided by BASF Construction Chemical Company. A sodium chloride solution (called an accelerator) is added to MasterRoc MP320 at the required ratio to obtain adequate gel times. The preparation of the accelerator consists of dissolving 10% by mass of salt in water. The characteristics of the product are shown in **Table 2**. The initial properties of colloidal silica are similar to those of water. **Fig. 7**a presents the gel time of MasterRoc MP320 with varying accelerator dosage. It makes evidence that higher dosage of accelerator results in shorter gel time. The results of diluted the colloidal silica before adjusting the accelerator are also presented in **Fig. 7**a. Gelification time increases with the decrease of the silica concentration in the mixture. To better visualize the fractures within the specimen during manual disassembling, a dye called Basacid® Blue 762 was added into the colloidal silica before injection (**Fig. 7**b). It is a water based anionic dye solution, allowing to inject into the sand specimen without any filtration.

4. Test procedure and specimen preparation

The test procedure consists of the following operations: fabrication and initial scan of the specimen using X-ray CT (Scan 1); saturation and application of the initial stress conditions; water injection by gradually increasing flow rate by steps until fracturing; colored gel injection to solidify the specimen after fracturing; second scan of specimen after fracturing using X-ray CT (Scan 2); and finally, manual disassembling and optical microscopy observation of the specimen. **Fig. 8** presents the configuration of the reconstituted specimen tested in this study which consists of three zones: the injection zone and two layers of lower permeability at the top and bottom. Two small membranes are placed between these layers (i.e., between injection zone and low permeability layer) in order to ensure full radial flow and prevent vertical flow out of the injection zone. These two layers of lower permeability contain 32% of C10 particles which is higher than the particles concentration of the injection zone (22% for the reference test). The specimen is prepared in dense state (density index of the NE34 sand matrix of 0.90).

The density index of the sand matrix $I_{D\ NE34}$ is defined as:

$$I_{D\ NE34} = \frac{e_{max}^{NE34} - e^{NE34}}{e_{max}^{NE34} - e_{min}^{NE34}} \quad (1)$$

where e_{max}^{NE34}, e_{min}^{NE34}, e^{NE34} are the maximum void ratio, the minimum void ratio and the void ratio of NE34 pure sand matrix (without fines).

By changing the concentration of C10 particles, we can change the permeability of the various layers of the specimen. Note that by keeping the same density index of the NE34 sand matrix and for the concentration of fine particles used in the tests, the structure of the sand pack remains unchanged (Cubrinovski and Ishihara, 2002). The characteristics of the reference specimen which contains 22% of C10 particles in the injection zone are presented in **Table 3**.

Fig. 9 shows the main steps of the specimen preparation. Firstly, some glass beads are glued on the lower plate as reference points, allowing to orient the scanned images in initial and post-fracturing states in the same position (**Fig. 9**a). The injection tube and drainage system are then fixed on the lower baseplate (**Fig. 9**b), followed by the installation of a 0.3 mm thick latex membrane and a cylindrical mold composed of two parts. The vacuum is then applied to press the membrane onto the mold (**Fig. 9**c). The mold is also made by PMMA to be compatible with X-ray CT scan (**Fig. 9**d). The specimens are reconstructed by dry compaction of ten layers of 2 cm using a groomer, specifically designed for this cell (**Fig. 9**e). After compacting the first lower permeability layer, a small latex membrane is placed on the top. This membrane is covered with grease to prevent any flow along its surface (**Fig. 9**f). Then, the injection zone of the specimen is built with eight layers and compacted and another small membrane is fixed on the top of the injection zone (**Fig. 9**g&h). The compacted surface of each layer is scarified prior to filling the following layer to avoid any artifacts due to manual compaction. When the compaction is done with the upper layer of lower permeability, a porous plastic disk is placed on the top of the specimen before setting up the upper baseplate (**Fig. 9**i).

Once the specimen is reconstituted, it is scanned using X-ray CT in order to build a reference 3D image of the specimen. After that, the cell is fixed to the Press Tri-SCAN (**Fig. 9**k). A vacuum of approximately -20 kPa is then applied to the specimen to take the mold out. The specimen is consolidated at an isotropic stress of 50 kPa before saturation (**Fig. 9**l). The saturation procedure consists of two steps. First carbon dioxide (CO_2) is circulated under a pressure of 20 kPa for 10 to 15 minutes in order to expel the air present in the pores and then de-aired water is injected by gravity through the central tube. After saturation is completed (Skempton coefficient B value > 0.9), the specimen is loaded to the desired stress conditions.

Tests are performed at controlled flow rate. This procedure permits to reach the fracturing regime and to pursue the injection beyond the critical threshold corresponding to the maximum injection pressure (fracturing state) by further increase of the flow rate. Various values of the maximum imposed flow rate can be chosen in order to reach various extents of the fractures. During the water injection phase, the flow rate is increased until the fracturing of the specimen corresponding to the first sharp drop of the pore pressure measured by the inlet pressure transducer. The injection rate is gradually increased by steps of 0.033 l/min. Each rate is maintained for approximately 1.5 minutes until the pressure stabilizes. When the first pressure drop occurs, the corresponding flow rate is maintained for 10 minutes before further increase. Three more injection steps are carried out before decreasing the injection rate to zero.

The gelling solution is prepared by manually mixing the colloidal silica MasterRoc MP320, the accelerator and 0.2% of Basacid Blue 762. Then, the the colored gel is immediately injected in order to avoid the undesired effect of an increase of the viscosity of the gel after adding the accelerator. The

injected volume of the gelling solution is about 50% of the voids volume of the specimen. The specimen is kept for few days under the stress conditions to solidify.

Once the specimen is solidified by the injected gel, the applied stresses are released and the mold is reinstalled to protect the specimen. Then, it is placed in the X-ray CT for scanning (Scan 2). After scanning the specimen, a second step of disassembling is performed which consists of a horizontal excavation of the specimen. In addition, a small part of the specimen containing a fracture is observed by optical microscopy to characterize the microstructure of the fracture at the grain scale.

5. Typical experimental results

In this section, the results of a reference test carried out in the radial injection cell are presented. First, we introduce the results during the water injection phase. Then, we present the observation of the specimen using different methods such as X-ray CT, manual excavation and optical microscopy. The main characteristics of this test are presented in **Table 4**.

5.1 Water injection phase

The pore pressure measurements are shown in **Fig. 10**a in which P_1 and P_2 are the measured pressure by the inlet and outlet pressure transducers (T1 and T2), respectively. The injection phase is performed in about 90 minutes. As the outlet pressure transducer is installed at the end of outlet pipe, P_2 is at atmospheric pressure. In the matrix injection regime, we observed the gradual increase of the injection pressure at constant imposed flow rate (**Fig. 10**b). This phenomenon can be attributed to internal erosion corresponding to the migration and filtration of a certain amount of fine particles (C10) inside the specimen. These mobilized particles accumulate in the pore throats, causing a local clogging of the specimen, and consequently a decrease of the overall permeability. Similar observations have been also made by Xiao and Shwiyhat (2012). To limit this phenomenon, before reaching the fracturing regime, the injection time of each step is fixed to only 1.5 minutes. When the flow rate reached 0.9 l/min, the first pressure drop was observed and the corresponding peak pressure measured by the inlet pressure transducer was 490 kPa. This flow rate step was maintained for 10 minutes, and then the flow rate was further increased with three more steps: 0.93 l/min, 0.96 l/min and 1 l/min before decreasing the flow rate until stop pumping (**Fig. 10**c). In the frac-regime, increase of the flow rate always leads to pressure drops at the beginning of the step followed by the gradual decrease of the pressure which are the signs of the propagation of fractures within the specimen.

As the pressure transducers are installed outside of the specimen, one has to account for the loss of hydraulic head in the driving line (flexible connection tube of 4 mm in internal diameter, valve, hydraulic tee fitting) to evaluate the pore pressure in the injection zone of the specimen. The loss of hydraulic head caused by the drainage system was determined by performing a calibration test without the specimen. At a given flow rate, the pressure at the entrance of tube injection P_{in} can be calculated by subtracting the pressure loss of the inlet driving pipe from the pressure measured by inlet pressure transducer P_1. In this device, the inlet pressure transducer was installed at the same vertical position as the cell, therefore the effect of the hydrostatic pressure is negligible.

Fig. 11 presents the test results in terms of pressure versus flow rate. This curve is plotted by using the corrected measurements of the pressure at the inlet of injection tube P_{in}. The critical fracturing pressure P_{frac} of 484 kPa corresponds to 2.42 times the confining pressure σ_h.

The permeability is calculated using Darcy's law for 2D radial flow, as:

$$k = \frac{\mu . Q}{\Delta P_s . 2 . \pi . h} \ln \frac{r_0}{r_1} \quad (2)$$

where : h is the height of injection zone, r_0 et r_1 are the radius of the injection tube and specimen, respectively, ΔP_s is the pressure drop by the specimen at the injection flow rate Q, μ is the dynamic fluid viscosity.

Due to internal erosion, the overall permeability of the specimen decreases from an initial value k_{int} of 82.8 to 66.6 mD at the end of the matrix regime (denoted by $k_{end,\,m}$). It is observed that at the end of the test (i.e. when the flow rate is decreased after fracturing), the overall permeability is k_{unload} 87.4 mD. Comparing the permeability at the end of the matrix regime $k_{end,\,m}$, and at the end of the test k_{unload} permits to assess that the gain of permeability due to fracturing is of 31%.

5.2 Observations of the specimen after fracturing.

The specimen was imaged before injection (Scan 1) and after fracturing (Scan 2). **Fig. 12**a presents a view of X-ray CT scanning of the specimen. The voxels are cubic with a size of 29 µm. The 3D images are reconstructed using X-Act software (RX-Solutions, Chavanod, France). Some typical horizontal cuts of the X-ray CT images are presented in **Fig. 12**. Compared to the initial state (Scan 1), the images of the fractured specimen (Scan 2) show some darker bands developed around the injection tube which indicate the localized fractures.

In order to visualize the 3D shape of the fractures, image processing was applied in the X-ray CT images which consists of three principal steps. Firstly, the filtering was applied to reduce the noise of the images while keeping the contours between different phases. Then, thresholding was performed to obtain the binary image that distinguishes between the fracture and the surrounding medium. Finally, the volume rendering was made to display a three-dimensional (3D) view of the fracture along the tube by using the ImageJ 3D Viewer plugin (Schmid et al., 2010). This process was carried out on a volume extracted at the middle of the specimen from H = 10 to H = 12 cm which is delimited by the window in dashed line presented in **Fig. 12**e. Multiple small fractures were observed in several directions around the injection tube which can be related to the pressure drops during the water injection phase (**Fig. 13**). Similar fractures geometry has been also observed in tests performed by Bohloli and de Pater (2006)

Fig. 14 presents some typical photos of the specimen during excavation after the test. Some small fractures were observed along the injection tube (darker blue) which are fairly consistent with those observed in the X-ray CT image. The length of these fractures varies from few millimeters up to one centimeter with an opening of about one millimeter (i.e. 5 grains size).

Moreover, in order to identify the change of the granular structure, a typical horizontal cross-section at H = 8 cm was observed using optical Microscope Leica M80 (**Fig. 15**a). The fracture is clearly identified as a darker blue zone visible to the naked eye (**Fig. 15Fig. 14**b). As the silica gel is a transparent gel with nano-particle size between 7 and 22 nm, it allows to observe the sand structure inside the gel. We can clearly observe that the fracture presents fewer C10 particles and more porous space as compared to the surrounding medium (**Fig. 15**c&d). It can be seen that during fracturing when the injection pressure and drag force locally become greater than a critical threshold, the dilation of the sand matrix occurred in some localized zones around the injection point where the injection pressure was highest. This phenomenon is attributed to a higher pore network within these zones leading to the detachment of C10 particles from the sand matrix and transport by the fluid flow. Therefore, a preferential path ('pseudo-crack') of high porosity is created favoring the injectivity. Thus, these pseudo-cracks appear as zones of higher porosity, higher pore size, in which finer particles have been mobilized

and transported by the fluid. These observations highlight the main differences between fracturing of an unconsolidated medium and fracturing of quasi-brittle materials. Fracturing of quasi-brittle materials is the result of two subsequent processes: localization of damage corresponding to crack initiation and crack propagation controlled by the stress intensity factor at the crack tip. Fracturing of unconsolidated medium is controlled not only by the stress state (that controls strain localization and dilatancy inside the specimen), but also by the flow rate (which controls the fine particles transport and deposition).

6. Sensitivity analysis

To highlight the key factors controlling the initiation of the fracture and the fracturing mode, a series of tests was carried out. The characteristics of these tests are summarized in **Table 5**. The effects of various parameters such as stress conditions (confining pressure, stress ratio), permeability and flow rate on the critical fracturing pressure, the increase of the overall permeability as well as the fracture shape are explored.

6.1 Test repeatability and influence of the flow rate during the fracturing regime

Test P7 was performed under the same characteristics as the reference test P1. The injection protocol in the matrix regime is also similar to that of test P1 with the increase of the flow rate by steps of 0.033 l/min. However, in the fracturing regime, test P7 was carried out with 6 steps, instead of 4 steps as for test P1, to study the impact of the increase of the flow rate on the fracturing propagation within the specimen which is one of the most important parameters that the reservoir engineers can control for maintaining injectivity during the PWRI operation (Ochi et al., 2014). The first injection part of this test allows to evaluate the test repeatability in the radial injection cell in terms of the critical fracturing pressure. The detailed results of test P7 are presented in **Fig. 16**a. The first pressure drop was identified at a flow rate Q_{frac} of 0.85 l/min (Figure 3.20b) and the corresponding fracturing pressure P_{frac} is 462 kPa (2.3 σ_h). This critical pressure is about 5% smaller than the critical value obtained for test P1, confirming a very good test repeatability in the radial injection cell. The flow rate was then increased with five more steps up to 1.03 l/min before stop pumping (**Fig. 16**b). Significant pressure drops were identified in the frac-regime. **Fig. 16**c&d present the observation of different zones by optical microscopy. The results are similar to those observed for the reference test: less C10 fine particles and larger pore size are observed inside the fracture as compared to the surrounding medium.

Fig. 17 presents a comparison between tests P1 and P7. A fairly good consistency in terms of pressure – flow rate curve can be observed in the matrix flow regime (before the first pressure drop) (**Fig. 17**a). In the fracturing regime, we can observe that increasing further the flow rate results in further propagation and enlargement of the fracture (**Fig. 17**c&d). The fracture morphology in specimen P7 is characterized by vertical fractures propagating radially from the tube, with the longest even reaching the specimen boundary. This observation is in accordance with a higher increase of the overall permeability of test P7 as compared to P1 (**Fig. 17**b).

For the radial injection cell tests, the injection of 4 steps in the fracturing regime is a suitable protocol when performing the parametric study in this setup to avoid the boundary effect as observed in specimen P7.

6.2 Effect of stress conditions

6.2.1 Confining pressure

The confining pressure is one of the most important parameters controlling the fracturing process, therefore, many studies have been performed to investigate the effect of this parameter on hydraulic

fracturing in unconsolidated sands (Bohloli and de Pater, 2006; Golovin et al., 2010; Hurt, 2012). To investigate this effect, six tests have been performed with different values of the confining pressure (120, 150, 200 and 350 kPa) and different stress ratios $K_0 = \sigma_h/\sigma_v$ (0.33, 0.4 and 0.5). **Fig. 18**a presents the injection results in the case of $K_0 = 0.33$. Tests P2 and P4 have been performed with a confining pressure of 150 kPa and 200 kPa, respectively. We observe that a higher confining pressure leads to a higher critical fracturing pressure. The first pressure drop P_{frac} in test P2 (150 kPa of confining pressure) is 360 kPa and 435 kPa in test P4 (200 kPa of confining pressure). However, the ratio of the fracturing pressure over the confining pressure is very close for both tests (2.4 for test P2 and 2.2 for test P4).

Fig. 18b shows that a higher increase of the overall permeability is observed at lower confining pressure**.** As the specimen is manually compacted with the mixture of sand and fine particles, the initial overall permeability may be slightly different depending on the compaction process, the homogeneity of the mixture, the pore network, etc… During the disassembling phase of the experiment, test P2 with lower confining pressure presents longer fractures as compared to test P4 (**Fig. 19**). The main fracturing pattern observed in these tests is the non-symmetric bi-wing fractures propagating along the injection tube. Similar results are obtained for $K_0 = 0.4$ (**Fig. 18**c&d) and $K_0 = 0.5$ (**Fig. 18**e&f). **Fig. 20** presents a synthesis of the normalized fracturing pressure (P_{frac}/σ_h) under different stress conditions. The mean value of this quantity is 2.35 and the standard deviation is 0.1. The standard deviation is about 4% of the mean value, showing that the normalized fracturing pressure is not affected by the change of the stress conditions within the range tested here. Note that some authors have found that this ratio can significantly vary in the range of 3 to 20 depending on experimental setups, injection protocols as well as the rheology of the injection fluid (Bohloli and de Pater, 2006; Zhou et al., 2010; Hurt, 2012).

6.2.2 Stress ratio coefficient K_0

To investigate the effect of K_0 on the fracturing process, three tests with different values of the axial stress values σ_v (400, 500, 600 kPa) while keeping the same confining pressure constant (200 kPa) have been performed. The results are shown in **Fig. 21**, and show that the stress ratio coefficient has a negligible effect on the fracturing pressure P_{frac}. A slight difference of this ratio is within the repeatability of the test. Test P4 with a higher axial stress presents the smallest fracturing pressure and smallest increase of the overall permeability.

6.3 Effect of the initial permeability

Different scenarios of the extension and the nature of the clogged area due to PWRI can lead to different values of the permeability around the injection point. To investigate the effect of the permeability of the specimen, test P8 with a specimen containing only 19% of C10 fines (as compared to 22% for the reference test) was performed. The stress conditions are similar to those of P6 ($\sigma_h = 120$ kPa and $\sigma_v = 300$ kPa). The injection rate is gradually increased by step of 0.066 l/min (instead of 0.033 l/min for the other tests with 22% C10), in order to have the same pressure steps in the specimen during each corresponding flow rate step. **Fig. 22**a&b present the results in the matrix regime of tests P6 and P8, respectively. Each increase of the flow rate corresponds to an increase of about 20 kPa of the injection pressure for both tests. **Fig. 22**c shows a comparison of the two tests in terms of pressure – flow rate curves. The critical fracturing pressures P_{frac} are very close (about 2.4 to 2.5 times the confining pressure). A higher increase of the permeability is observed in the case of lower concentration of C10 fines (higher initial permeability). However, it should be noted that test P8 was performed with higher increase of each flow rate steps which may also contribute to the higher increase of the permeability. The observation of the fracture shape during excavation allows to confirm the change of the overall permeability during injection (**Fig. 22**e&f). Higher increase of the permeability after fracturing is associated to longer and wider fractures.

7. Conclusions

A new experimental setup has been developed which allows to simulate the radial injection configuration of injection wells for investigating fracturing mechanisms in unconsolidated sand reservoirs. This device makes possible observations of the entire specimen by X-ray CT while keeping the structure intact before and after fracturing. Specimens are prepared as a mixture of silica sand and fine silica particles to simulate the internal cake formed during PRWI operations.

Typical injection results show that the fracturing occurs at a critical injection pressure of about 2.4 times the confining pressure. After fracturing, the overall permeability of the specimen increases. The injection of a silica gel permits to freeze the structure of the fractured specimen for performing post-mortem observations of the specimen. X-ray CT allows to obtain 3D images of the fractures formed along the injection tube and the fractures observed from X-ray CT coincide with those observed during disassembling and excavation of the specimen. These vertical fractures are short with multiple small branches propagating radially from injection tube which can be associated with the pressure drops identified during water injection phase. Optical microscopic observations of the specimen after the tests have permitted to identify the dominant fracturing mechanisms in the sand specimen. The pseudo-cracks appear as zones of higher porosity and higher pore size which result from the formation of localized dilation shear bands in the sand matrix and the subsequent transport of finer particles.

The sensitivity analysis shows that the critical fracturing pressure is mainly controlled by the confining pressure (radial stress) and does not change significantly with the stress ratio K_0. Increase of confining pressure leads to the proportional increase in critical fracturing pressure, shorter fractures as well as smaller increase of the overall permeability. For all the tests performed, the mean of the normalized fracturing pressure is about 2.35 ± 0.1. Further increase the flow rate in the fracturing regime leads to extend the fractures, and consequently, contributes to higher gain of the overall permeability. Changing the concentration of C10 fines in the specimen permits to change the initial permeability of the specimen. However, no significant effect of the initial permeability on the critical fracturing pressure has been observed. For unconsolidated sand specimens, the fracturing pattern is difficult to predict with the growth of multiple or unsymmetrical bi-wing fractures as observed in this work. Future work will extend this research to investigate the effect of the injection scenario, of the viscosity of fluid, and the presence of suspended particles in the injected fluid on the fracturing response of the sand formations.

Declaration of competing interest

The authors declare no competing financial interest.

Acknowledgements

The authors gratefully acknowledge Total for financial support and permission to publish this work. They are also grateful to Baptiste Chabot and Marine Lemaire for their invaluable contribution during development of the new injection device and to Dr. Michel Bornert and Dr. Patrick Aimedieu for their useful comments and suggestions for the Xray-CT study.

References

Al-Abduwani, F.A.H., Shirzadi, A., van den Broek, W.M.G.T., Currie, P.K., 2005. Formation damage vs. solid particles deposition profile during laboratory-simulated produced-water reinjection. SPE J. 10, 138–151. https://doi.org/10.2118/82235-pa

Ameen, S., Taleghani, A.D., 2015. Dynamic modeling of channel formation during fluid injection into unconsolidated formations. SPE J. 689–700.

Bautista, J.F., Taleghani, A.D., 2018. Prediction of formation damage at water injection wells due to channelization in unconsolidated formations. J. Pet. Sci. Eng. 164, 1–10. https://doi.org/10.1016/j.petrol.2017.12.073

Bohloli, B., de Pater, C.J., 2006. Experimental study on hydraulic fracturing of soft rocks: Influence of fluid rheology and confining stress. J. Pet. Sci. Eng. 53, 1–12. https://doi.org/10.1016/j.petrol.2006.01.009

Chang, H., 2004. Hydraulic fracturing in particulate materials. Georgia Institute of Technology.

Chudnovsky, A., Shulkin, Y., Golovin, E., Zhang, H., Dudley, J.W., Wong, G.K., 2015. Observation and modeling of fluid flow under matrix and fracturing injections in unconsolidated sand, in: 49th US Rock Mechanics / Geomechanics Symposium 2015. OnePetro.

Cubrinovski, M., Ishihara, K., 2002. Maximum and minimum void ratio characteristics of sands. Soils Found. 42, 65–78.

de Pater, C.J., Dong, Y., 2009. Fracture containment in soft sands by permeability or strength contrasts, in: SPE Hydraulic Fracturing Technology Conference. OnePetro, pp. 685–693. https://doi.org/10.2118/119634-ms

de Pater, C.J., Dong, Y., 2007. Experimental study of hydraulic fracturing in sand as a function of stress and fluid rheology, in: SPE - Hydraulic Fracturing Technology Conference. OnePetro. https://doi.org/10.2118/105620-ms

Detournay, E., 2016. Mechanics of Hydraulic Fractures. Annu. Rev. Fluid Mech. 48, 311–339. https://doi.org/10.1146/annurev-fluid-010814-014736

Dong, Y., 2010. Hydraulic fracture containment in sand. Delft University of Technology.

Economides, M.J., al., E., 2007. On the problem of fluid leakoff during hydraulic fracturing. Transp. Porous Media 67, 487–499. https://doi.org/10.1007/s11242-006-9038-7

Farajzadeh, R., 2004. Produced water re-Injection (PWRI): An experimental investigation into internal filtration and external cake build up. Delft Univ. Technol.

Feia, S., Dupla, J.C., Canou, J., Ghabezloo, S., Sulem, J., Chabot, B., Aubry, E., Mainguy, M., 2017. An experimental setup with radial injection for investigation of transport and deposition of suspended particles in porous media. Geotech. Test. J. 40. https://doi.org/10.1520/GTJ20160032

Feia, S., Dupla, J.C., Ghabezloo, S., Sulem, J., Canou, J., Onaisi, A., Lescanne, H., Aubry, E., 2015. Experimental investigation of particle suspension injection and permeability impairment in porous media. Geomech. Energy Environ. 3, 24–39. https://doi.org/10.1016/j.gete.2015.07.001

Fjar, E., Holt, R. M., Raaen, A. M., & Horsrud, P., 2008. Petroleum related rock mechanics, Elsevier.

Gallagher, P.M., Lin, Y., 2009. Colloidal Silica Transport through Liquefiable Porous Media. J. Geotech. Geoenvironmental Eng. 135, 1702–1712. https://doi.org/10.1061/(asce)gt.1943-5606.0000123

Germanovich, L.N., Hurt, R.S., Ayoub, J.A., Siebrits, E., Norman, W.D., Ispas, I., Montgomery, C., 2012. Experimental study of hydraulic fracturing in unconsolidated materials, in: SPE International Symposium and Exhibition on Formation Damage Control. OnePetro, pp. 931–945. https://doi.org/10.2118/151827-MS

Golovin, E., Chudnovsky, A., Dudley, J.W., Wong, G.K., 2011. Injection rate effects on waterflooding mechanisms and injectivity in cohesionless sand, in: 45th US Rock Mechanics / Geomechanics Symposium. OnePetro.

Golovin, E., Jasarevic, H., Chudnovsky, A., Dudley, J.W., Wong, G.K., 2010. Observation and characterization of hydraulic fracture in cohesionless sand, in: 44th US Rock Mechanics Symposium and 5th US-Canada Rock Mechanics Symposium. OnePetro.

Hurt, R.S., 2012. Toughness-dominated hydraulic fractures in cohesionless particulate materials. Georg. Inst. Technol. Georgia Institute of Technology.

Jasarevic, H., Golovin, E., Chudnovsky, A., Dudley, J.W., Wong, G.K., 2010. Observation and modeling of hydraulic fracture initiation in cohesionless sand, in: 44th US Rock Mechanics Symposium and 5th US-Canada Rock Mechanics Symposium. OnePetro.

Khodaverdian, M., McElfresh, P., 2000. Hydraulic fracturing stimulation in poorly consolidated sand: Mechanisms and consequences, in: SPE Annual Technical Conference and Exhibition. OnePetro. https://doi.org/10.2118/63233-MS

Li, Z., Wong, R.C.K., 2008. Estimation of Suspended Particle Retention Rate and Permeability Damage in Sandstone from Back Analysis of Laboratory Injection Tests, in: Canadian International Petroleum Conference. OnePetro.

Mahadevan, A., Orpe, A. V, Kudrolli, A., Mahadevan, L., 2012. Flow-induced channelization in a porous medium. EPL (Europhysics Lett. 98. https://doi.org/10.1209/0295-5075/98/58003

Mainguy, M., Perrier, S., Buré, E., 2020. Produced-Water Reinjection in Deep Offshore Miocene Reservoirs, Block 17, Angola. SPE Prod. Oper. 35, 292–307. https://doi.org/10.2118/197061-PA

Montgomery, C.T., Smith, M.B., Jr, C., Dollarhide, F.E., Elbel, J.L., Robert Fast, C., Hannah, R.R., Harrington, L.J., Perkins, T.K., Prats, M., van Poollen, H., 2010. Hydraulic fracturing: history of an enduring technology. J. Pet. Technol. 62, 26–40.

Ochi, J., Dexheimer, D., Corpel, P. V., 2014. Produced-water-reinjection design and uncertainties assessment, in: SPE Production and Operations. pp. 192–203. https://doi.org/10.2118/165138-PA

Onaisi, A., Ochi, J., Mainguy, M., Souillard, P., 2011. Modeling non-matrix flow and seals integrity in soft sand reservoirs, in: SPE European Formation Damage Conference. Society of Petroleum Engineers, pp. 1371–1387.

Papanastasiou, P., 1999. The effective fracture toughness in hydraulic fracturing. Int. J. Fract. 96, 127–147. https://doi.org/10.1023/A:1018676212444

Papanastasiou, P., 1997. The influence of plasticity in hydraulic fracturing. Int. J. Fract. 84, 61–79. https://doi.org/10.1023/A:1007336003057

Persoff, B.P., Apps, J., Moridis, G., Whang, J.M., 1999. Effect of dilution and contaminants on sand grouted with colloidal silica. J. Geotech. Geoenvironmental Eng. 125, 461–469.

Sarris, E., Papanastasiou, P., 2013. Numerical modeling of fluid-driven fractures in cohesive poroelastoplastic continuum. Int. J. Numer. Anal. Methods Geomech. 37, 1822–1846. https://doi.org/10.1002/nag

Schmid, B., Schindelin, J., Cardona, A., Longair, M., Heisenberg, M., 2010. A high-level 3D

visualization API for Java and ImageJ. BMC Bioinformatics 11.

Shutong, P., Sharma, M.M., 1997. A model for predicting injectivity decline in water-injection wells, in: SPE Formation Evaluation. pp. 194–201.

Souilah, R., Brocart, B., Ourir, A., Onaisi, A., Pourpak, H., Ochi, J., Lescanne, H., 2014. Produced water re-injection in a deep offshore environment-Angola block 17, in: SPE - European Formation Damage Conference, Proceedings,. OnePetro. https://doi.org/10.2118/168216-ms

Wong, G.K., Dudley, J.W., Golovin, E., Zhang, H., Chudnovsky, A., 2017. Injector completion performance under hydraulic fracturing and matrix flooding conditions into a sand pack, in: 51st US Rock Mechanics / Geomechanics Symposium 2017. OnePetro.

Wu, R., 2006. Some fundamental mechanisms of hydraulic fracturing. Georgia Institute of Technology.

Xiao, M., Shwiyhat, N., 2012. Experimental investigation of the effects of suffusion on physical and geomechanic characteristics of sandy soils. Geotech. Test. J. 35, 1–11. https://doi.org/10.1520/GTJ104594

Zhai, Z., Sharma, M.M., 2005. A new approach to modeling hydraulic fractures in unconsolidated sands, in: SPE Annual Technical Conference and Exhibition. OnePetro.

Zhou, J., Dong, Y., de Pater, C.J., Zitha, P.L.J., 2010. Experimental study of hydraulic fracturing caused by polymer injection in unconsolidated heavy oil reservoirs, in: Society of Petroleum Engineers - International Oil and Gas Conference and Exhibition in China 2010, IOGCEC. OnePetro. https://doi.org/10.2523/131261-ms

List of Symbols

Symbol	Units	Definition
$I_{D\ NE34}$		Density index of the NE34 sand matrix
k	Darcy	Intrinsic permeability
K_0		Stress ratio coefficient
p	kPa	Pressure
P_1	kPa	Measured pressure by the inlet pressure transducer
P_2	kPa	Measured pressure by the outlet pressure transducer
P_{frac}	kPa	First drop pressure observed during fracturing regime
P_{in}	kPa	Pressure at the entrance of injection tube
q	l/min	Flow rate
Q_{frac}	l/min	Flow rate corresponding to the first drop pressure
t	min	Time
ΔP_s	kPa	Pressure loss in the specimen
σ_h	kPa	Confining pressure
σ_v	kPa	Axial stress

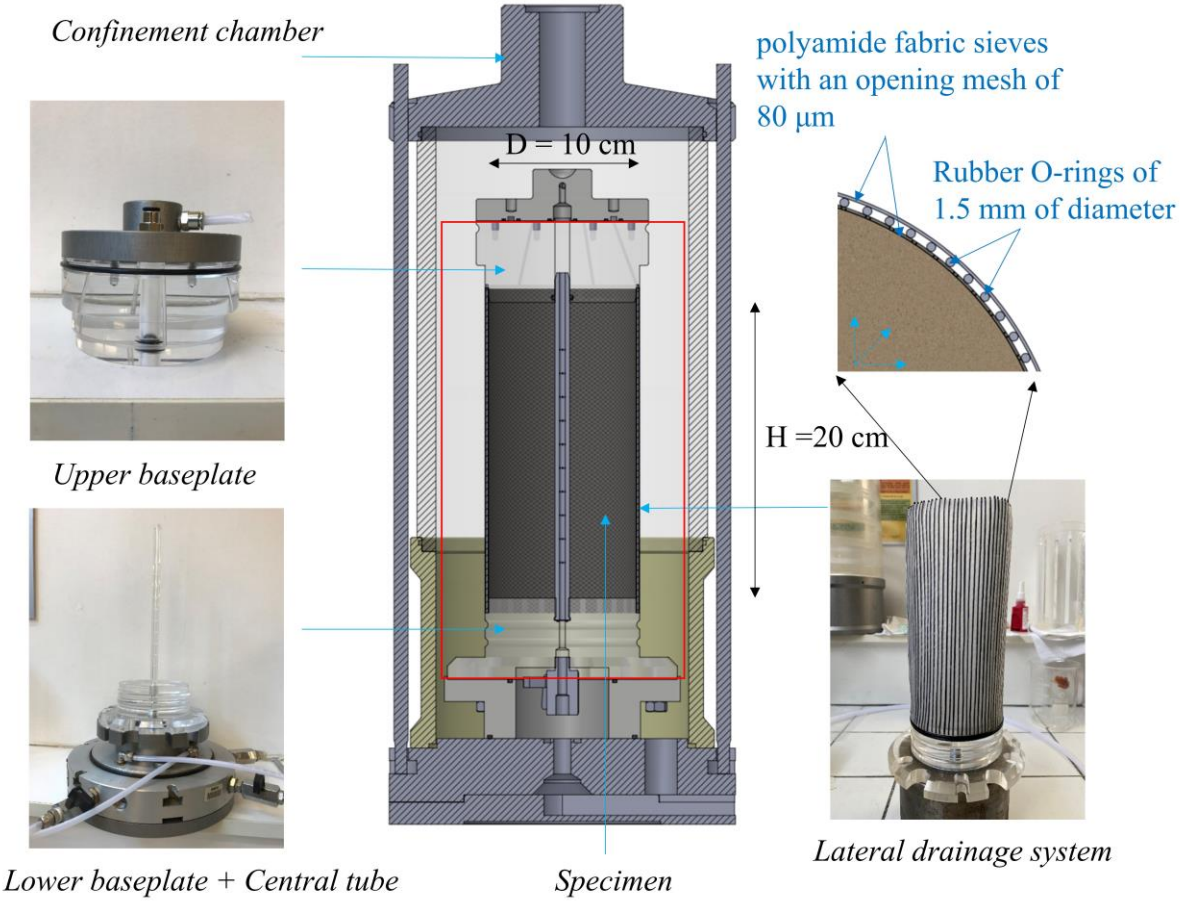

583

584 **Fig. 1.** 2D cross section of the radial injection cell and its corresponding components.

585

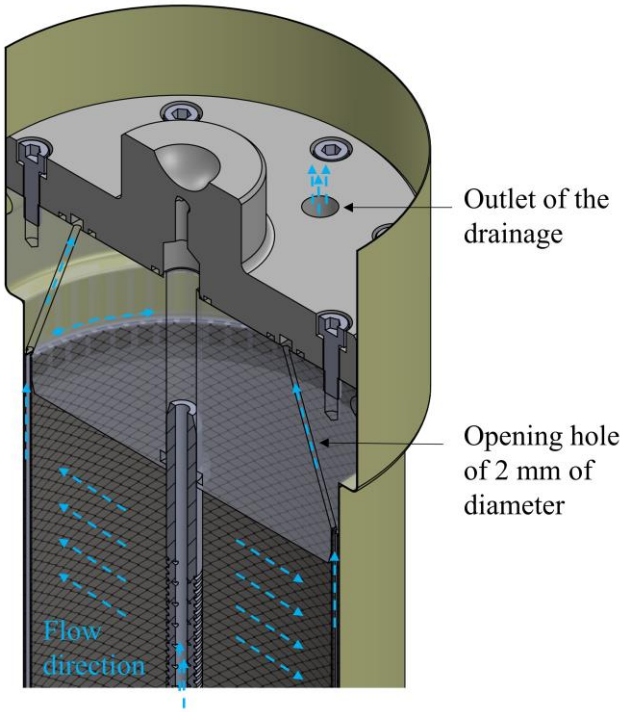

586

587 **Fig. 2.** 3D schematic cross-section representing the flow direction within the radial injection cell.

588

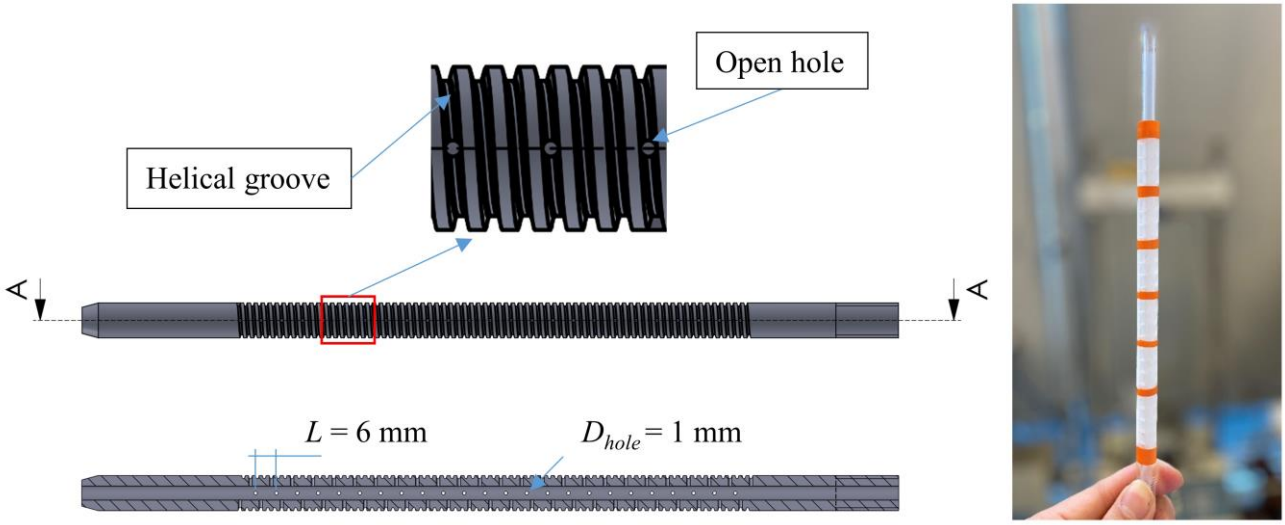

589

(a) (b)

590 **Fig. 3.** (a) configuration of injection tube; (b) view of the tube covered with polyamide fabric sieves.

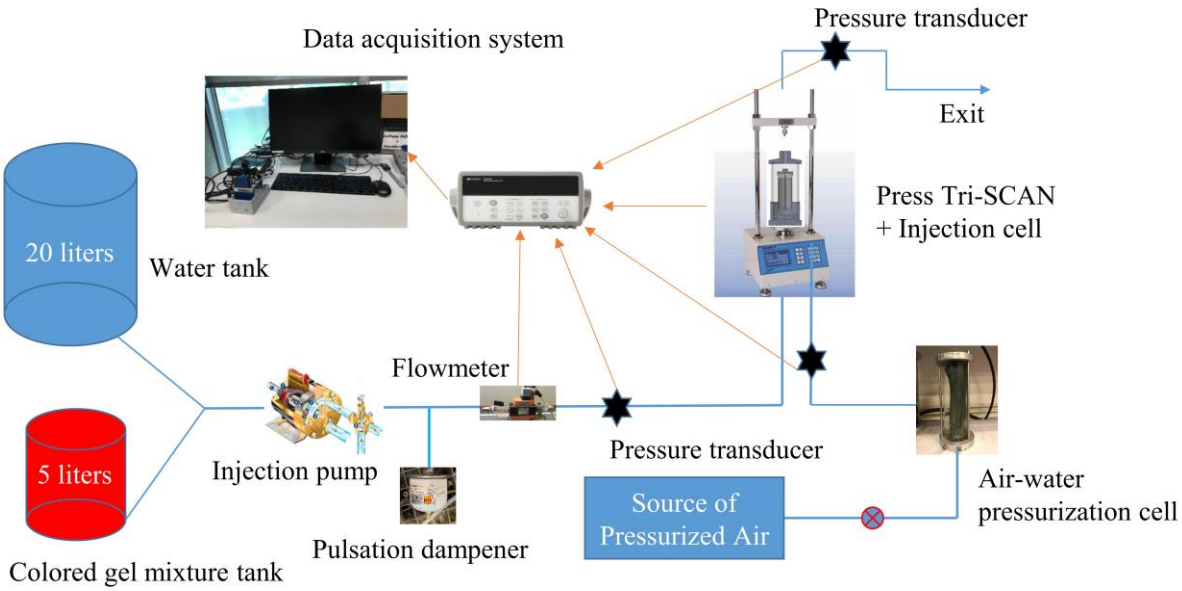

591

592 **Fig. 4.** Functional scheme of the radial injection cell setup.

593

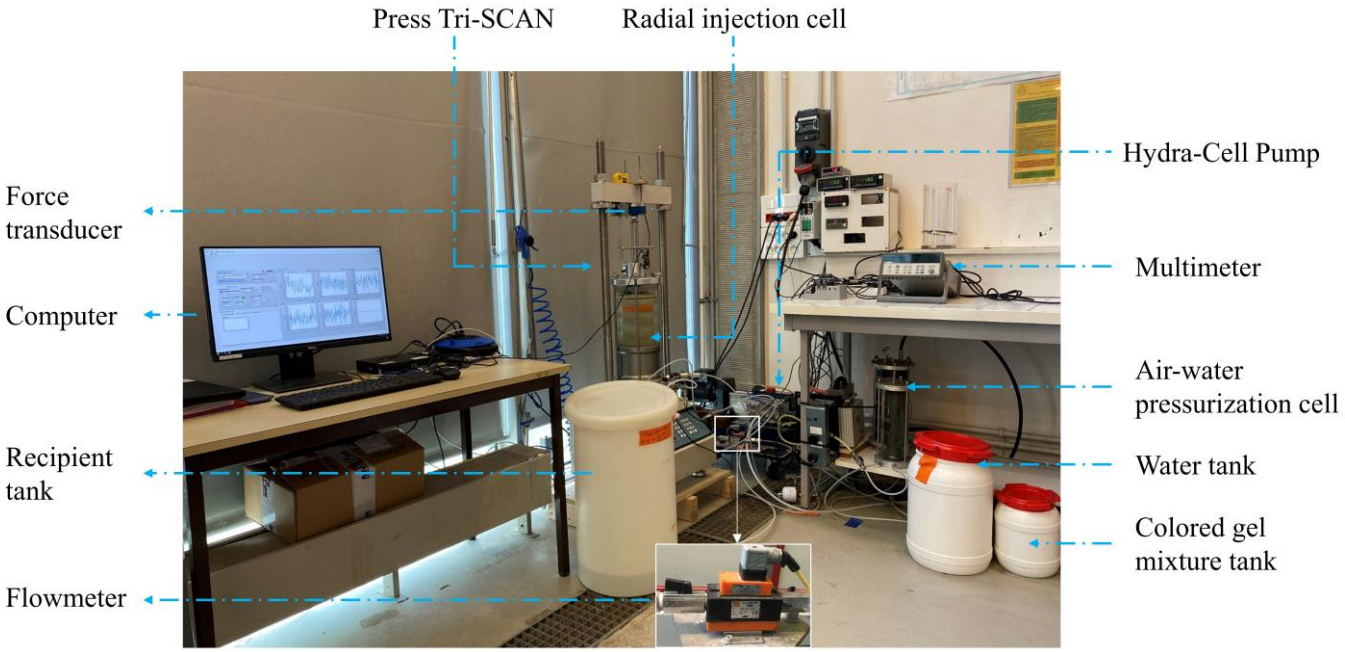

594

595 **Fig. 5.** General view of the radial injection cell setup.

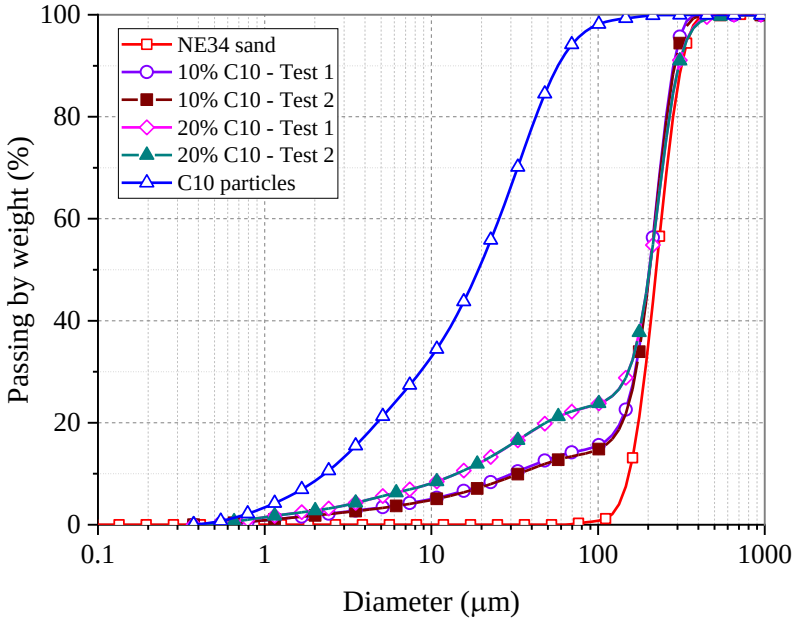

(a)

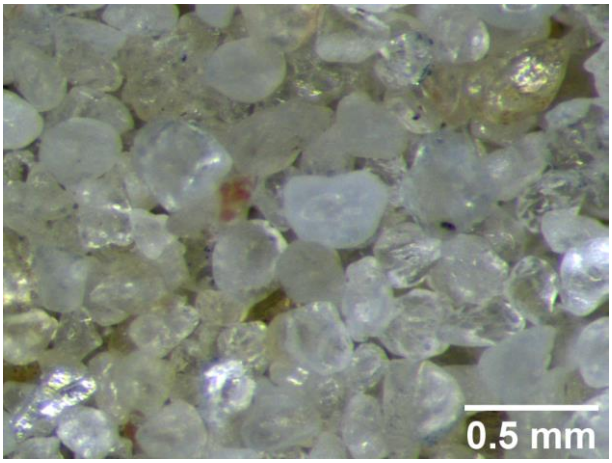

(b)

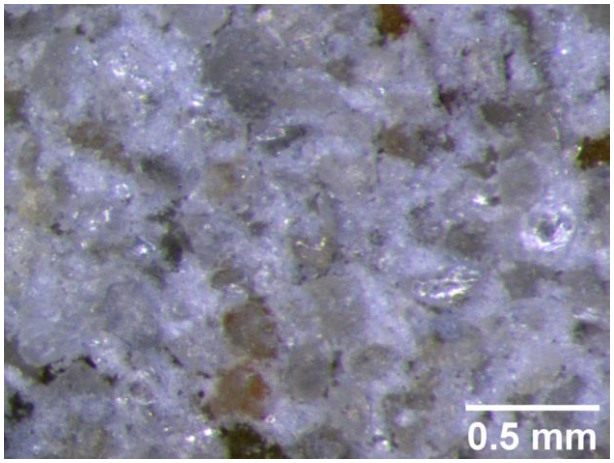

(c)

Fig. 6. Tested material: (a) grain size ditribution; (b), (c) optical microscopy views of pure NE34 sand and of the reference mixture (N34 sand + 22% C10), respectively.

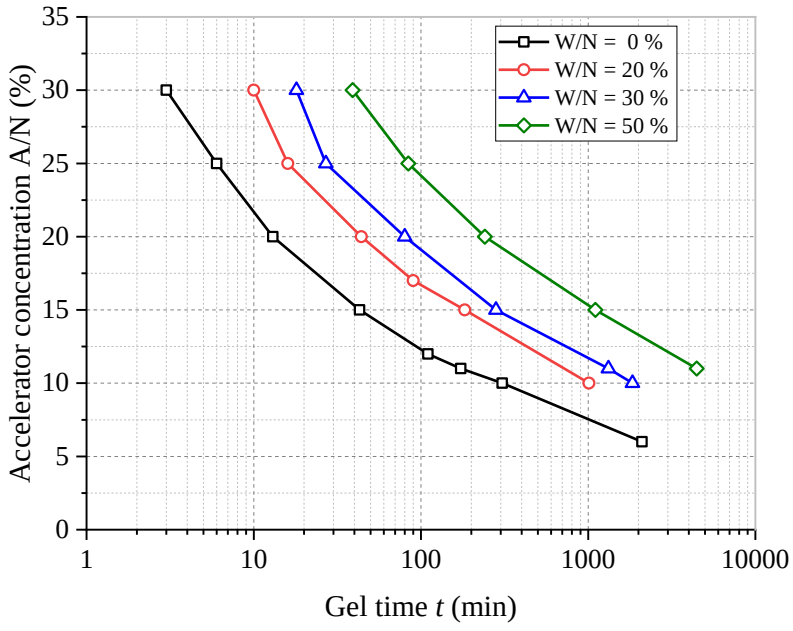

(a)

(b) 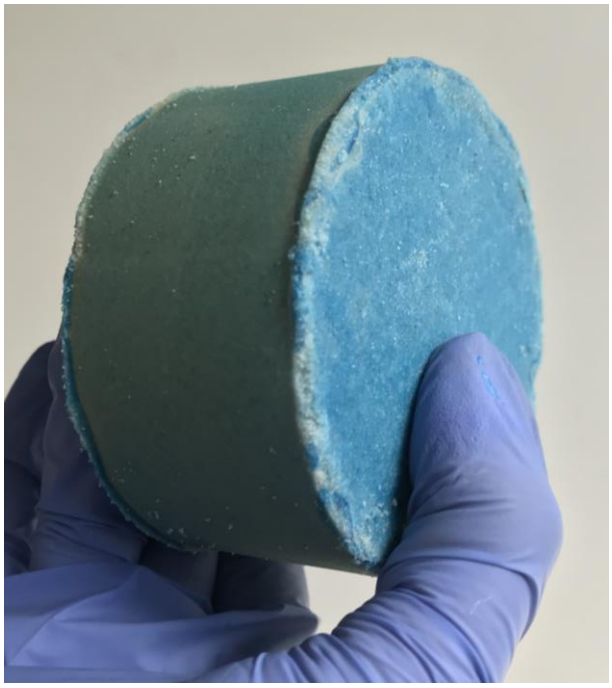

Fig. 7. Colored gel solution: (a) gel time of MasterRoc MP320 with different accelerator ratios and dilution ratios; (b) solidified sand specimen with the mixture of MasterRoc MP320 and Basacid® Blue 762.

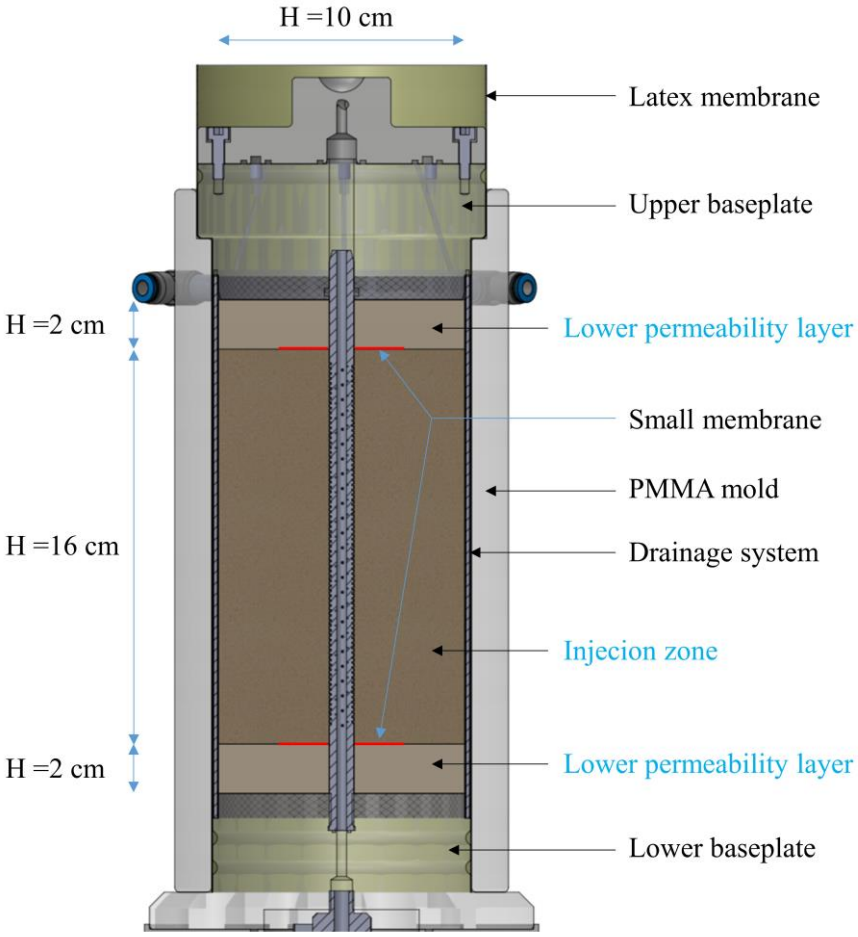

Fig. 8. Configuration of the specimen preparation.

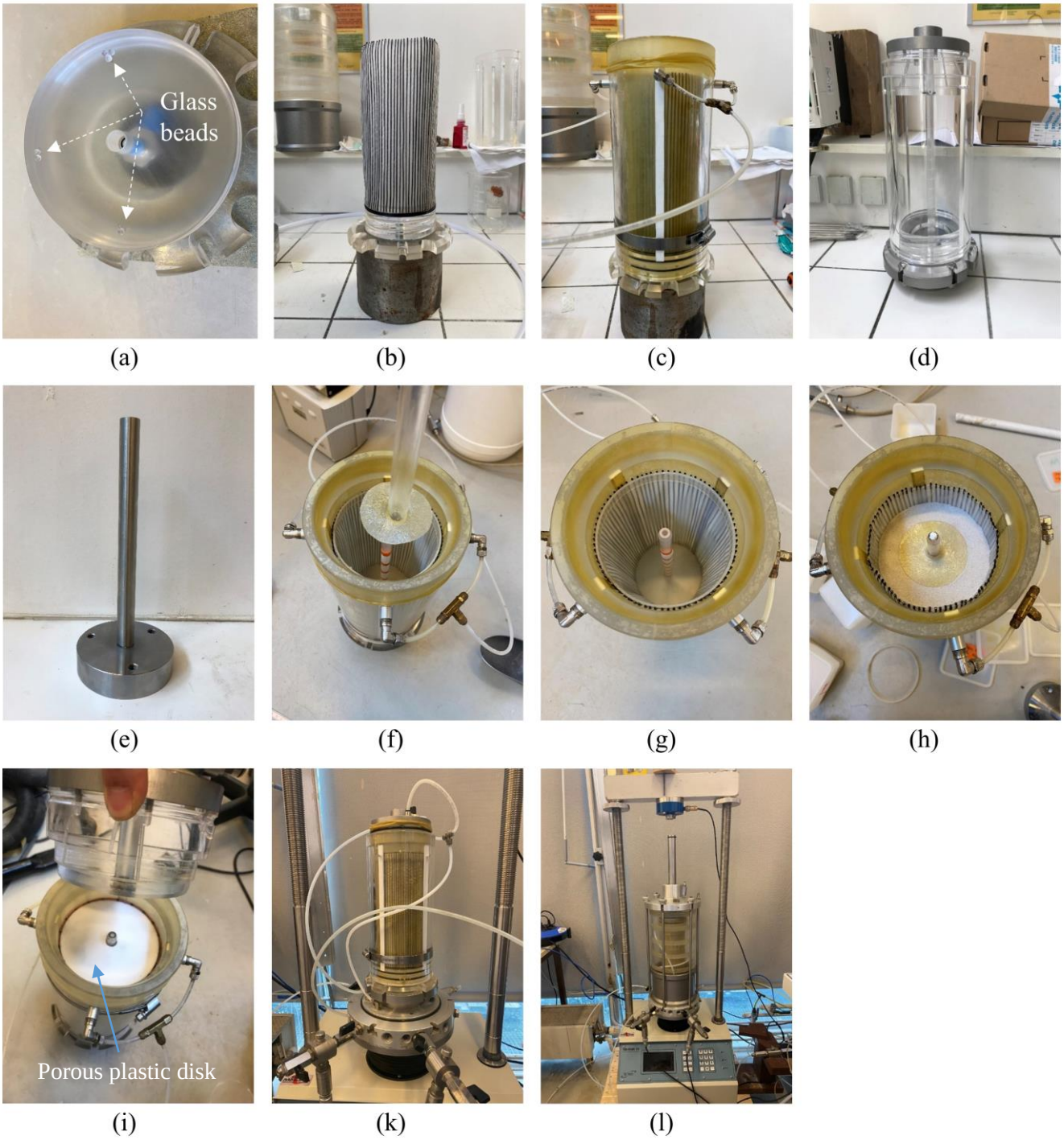

Fig. 9. Fabrication of the specimen and assembly of the injection cell: (a) glass beads glued to the lower plate; (b) lateral drainage system and injection tube setup; (c) pressing the membrane onto the mold; (d) PMMA mold; (e) groomer; (f) setting up a small latex membrane; (g) compaction of the injection zone; (h) second small membrane; (i) upper base plate; (k) fixing the cell to the Press Tri-SCAN; (l) saturation.

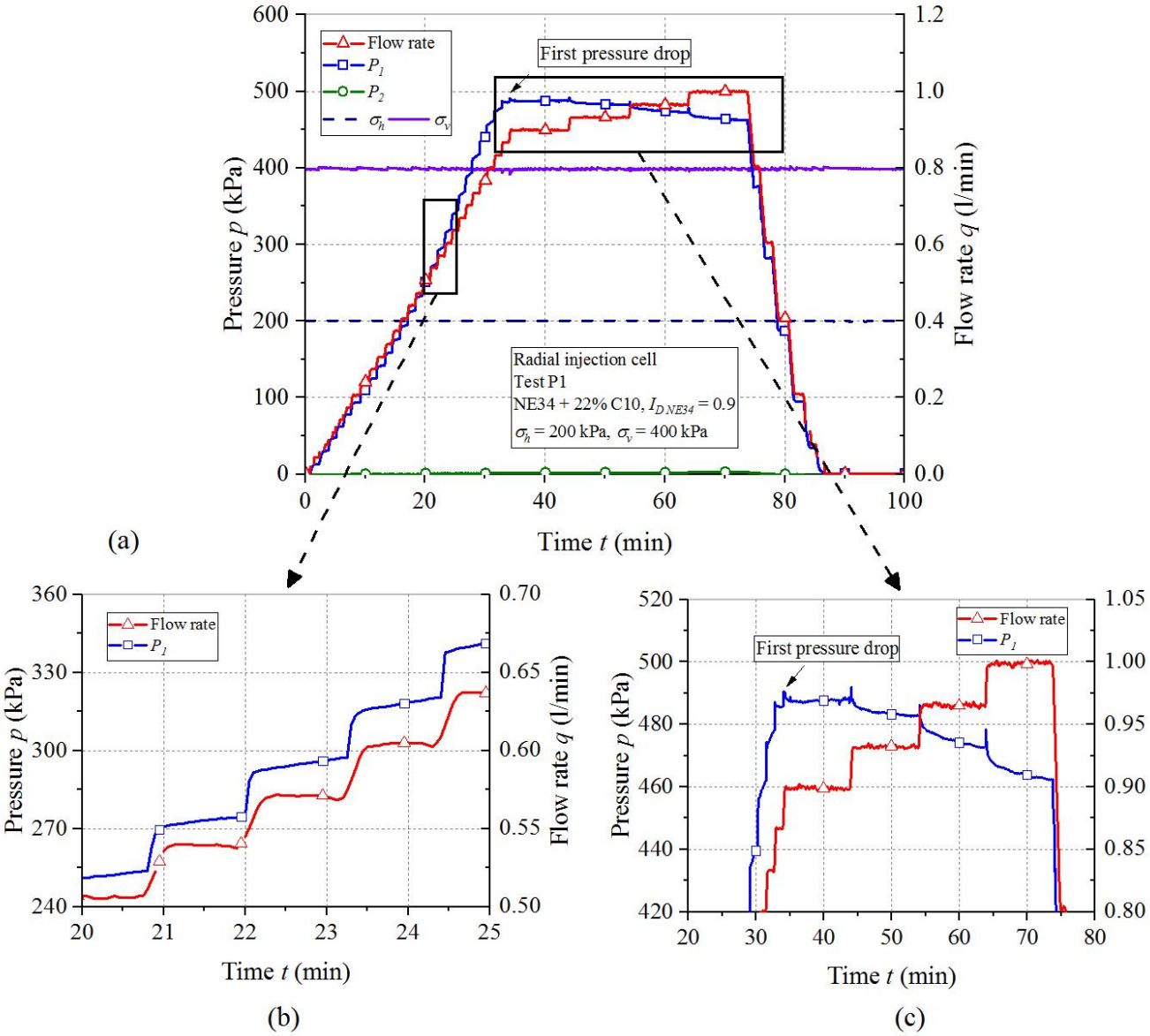

Fig. 10. Results of the reference test P1: (a) evolution of pressure and flow rate versus time during water injection phase; (b) zoom between 20 to 25 minutes showing the injection pressure during matrix regime; (c) zoom between 30 to 80 minutes showing significant pressure drops during fracturing regime.

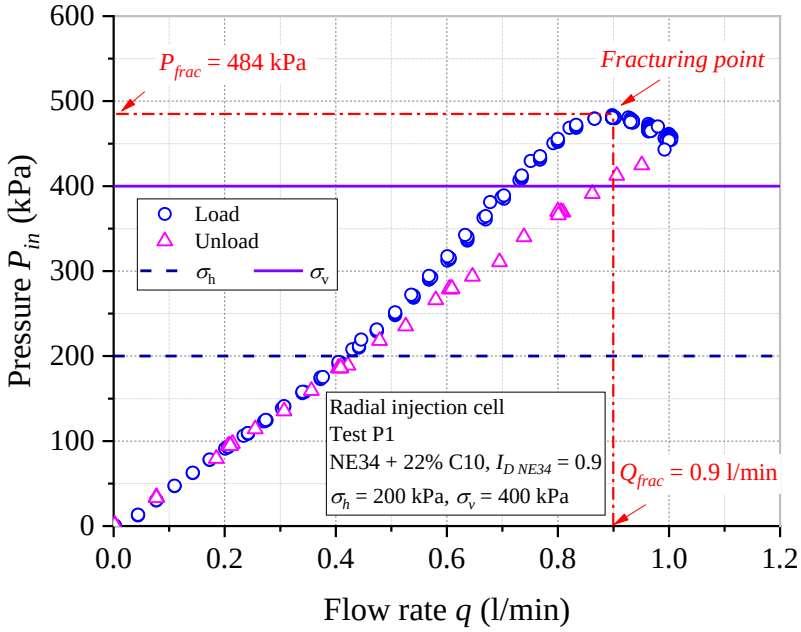

622

623 **Fig. 11.** Evolution of injection pressure versus flow rate.

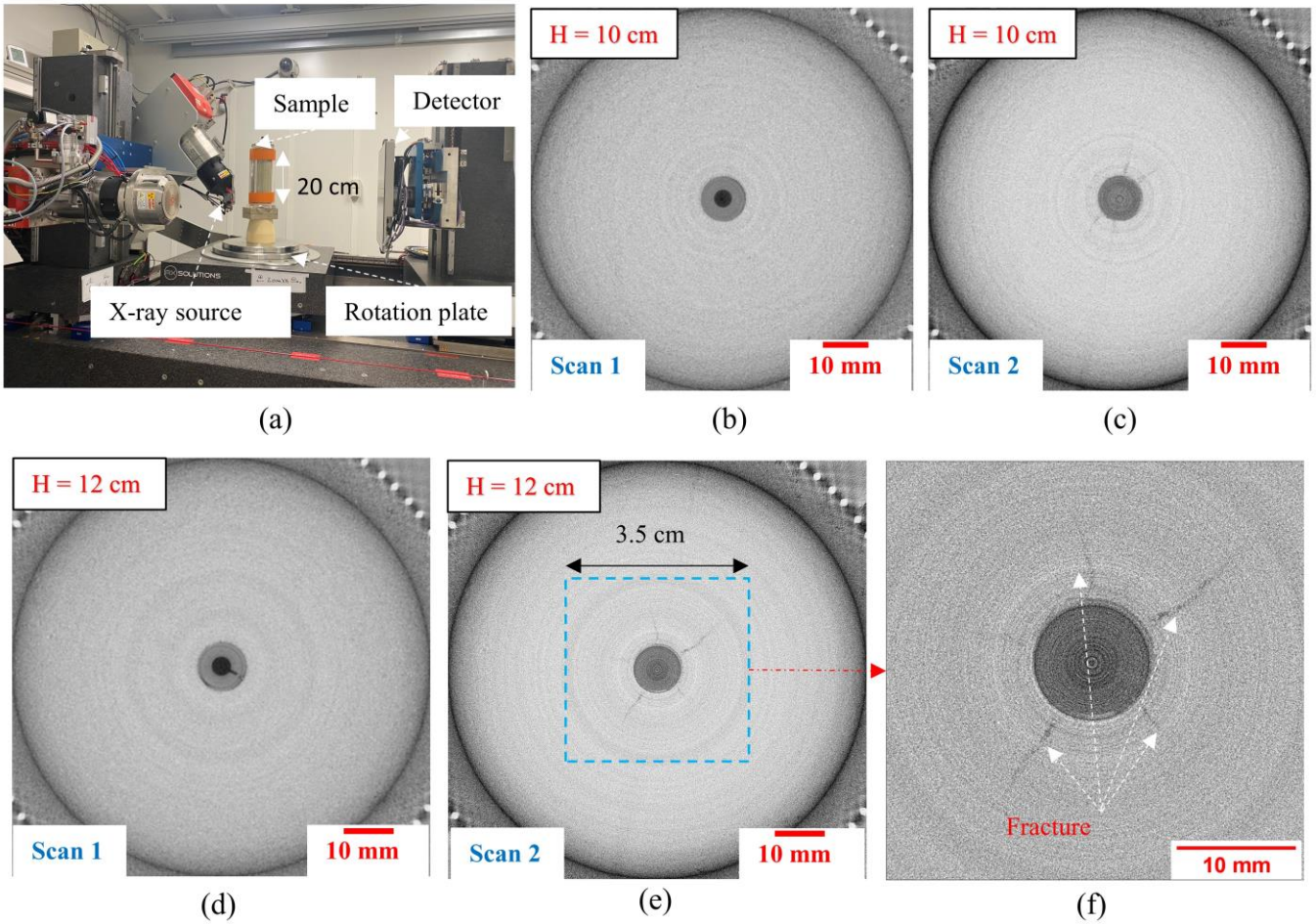

624

625 **Fig. 12.** Typical X-Ray CT images at different heights: (a) Global view of the setting; (b) and (c)
626 cross-sections of the specimen before (scan 1) and after fracturing (scan 2) at H = 10 cm, (d) and (e)
627 cross-sections of the specimen before (scan 1) and after fracturing (scan 2) at H = 12 cm; (f) magnified
628 zone containing the fractures over which the image treatment process is applied. Voxel size: 29 µm.

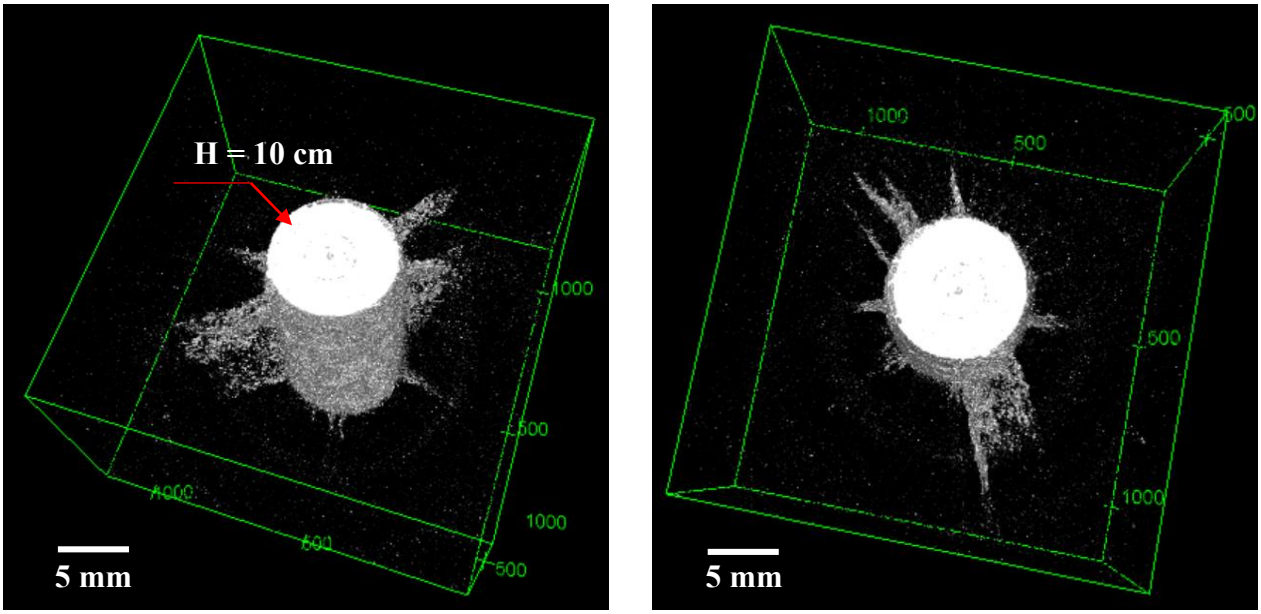

Fig. 13. 3D views of the fracture developed along the injection tube from H = 10 to H = 12 cm.

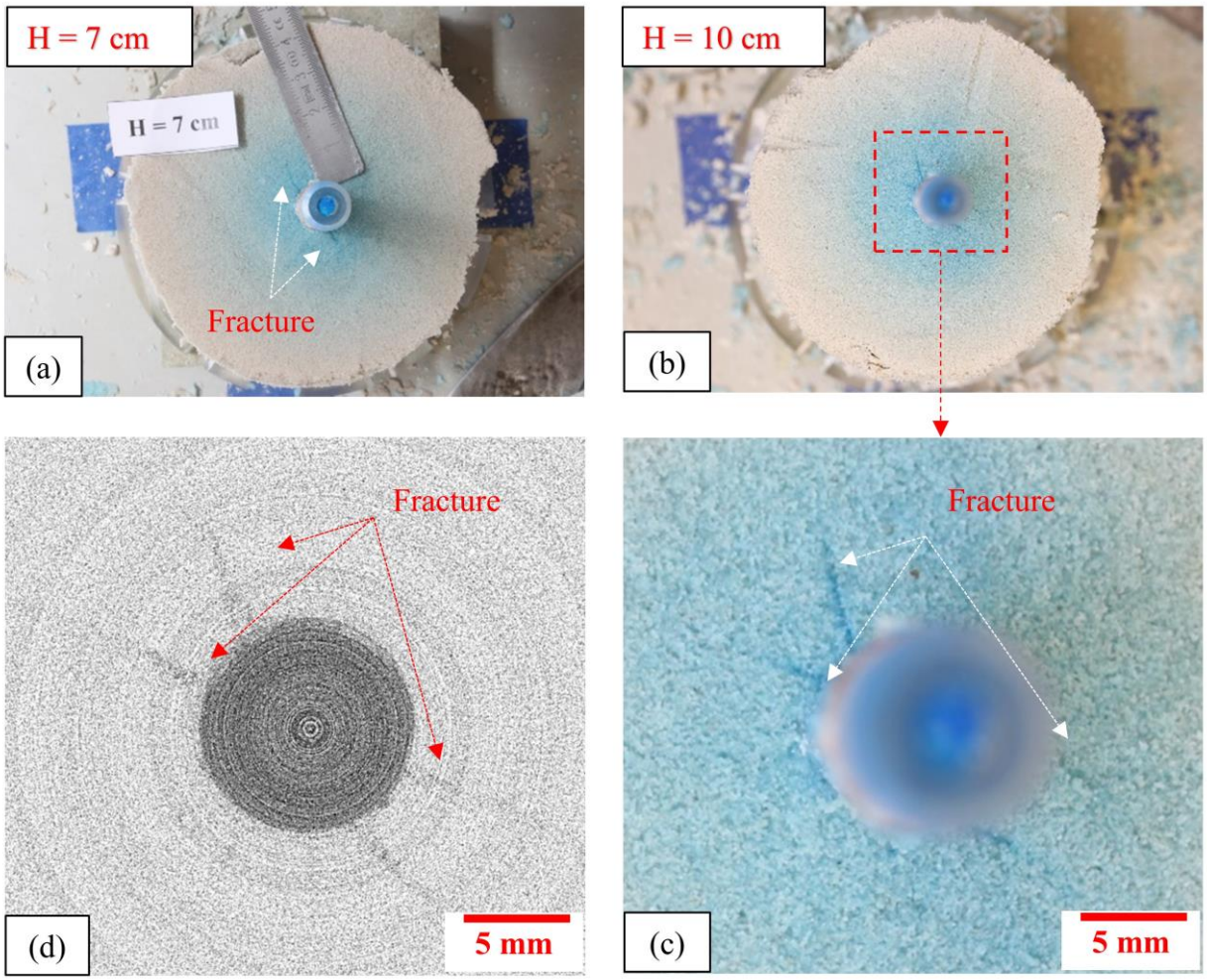

Fig. 14. Photos of the horizontal cross-sections corresponding to different depths of excavation: (a) at H = 7 cm; (b) at H = 10 cm; (c) magnified zone around the tube at H = 10 cm and (d) its observation from X-ray CT.

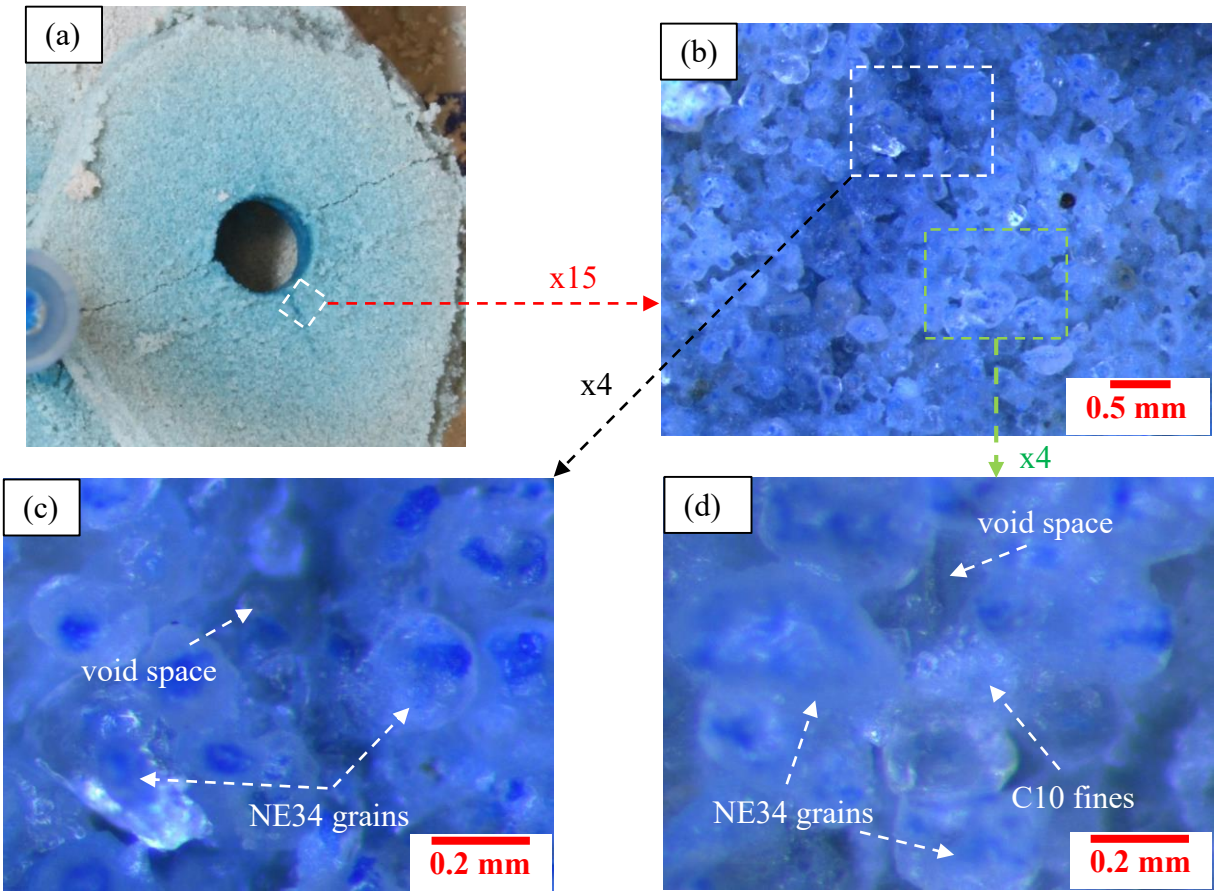

Fig. 15. Optical microscope observation of a typical transversal cross-section at different zones: (a) typical cross-section of the specimen; (b) magnified zone containing the fracture; (c) magnified zone inside the fracture; (d) magnified zone at the surrounding medium.

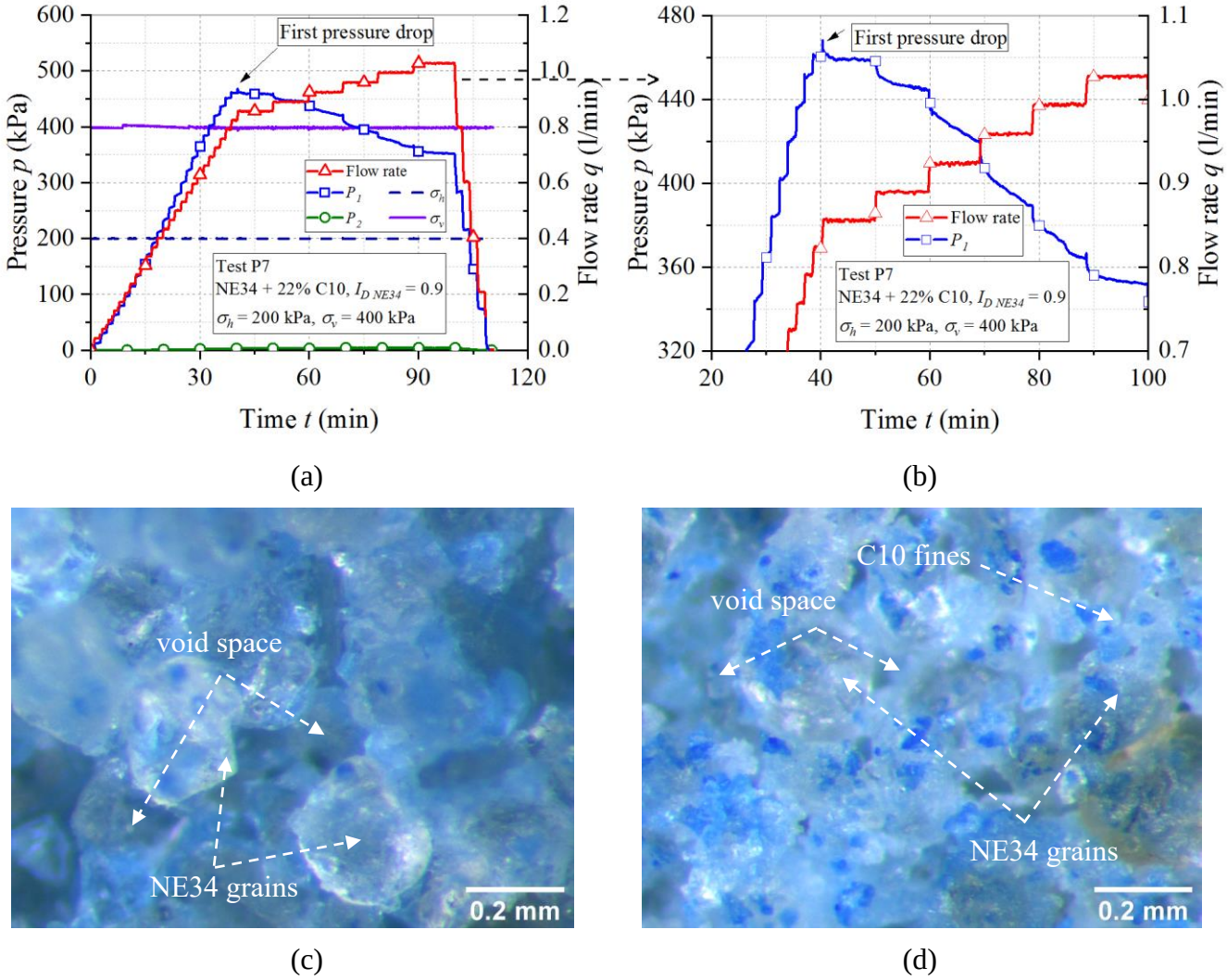

Fig. 16. Test P7: (a), (b) pressure - flow rate - time curves; (c) magnified zone inside the fracture; (d) magnified zone in the surrounding medium.

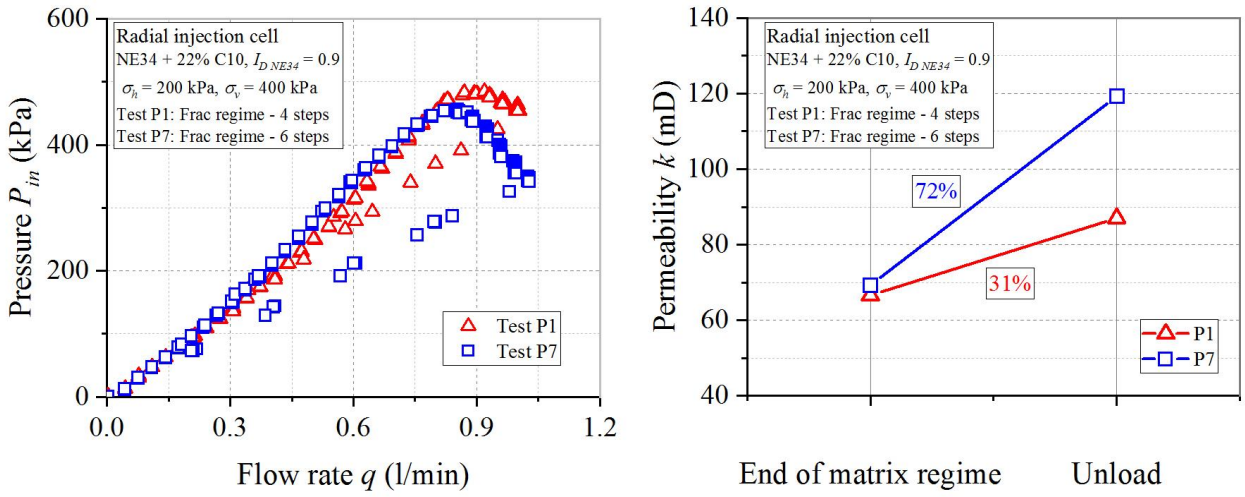

(a) (b)

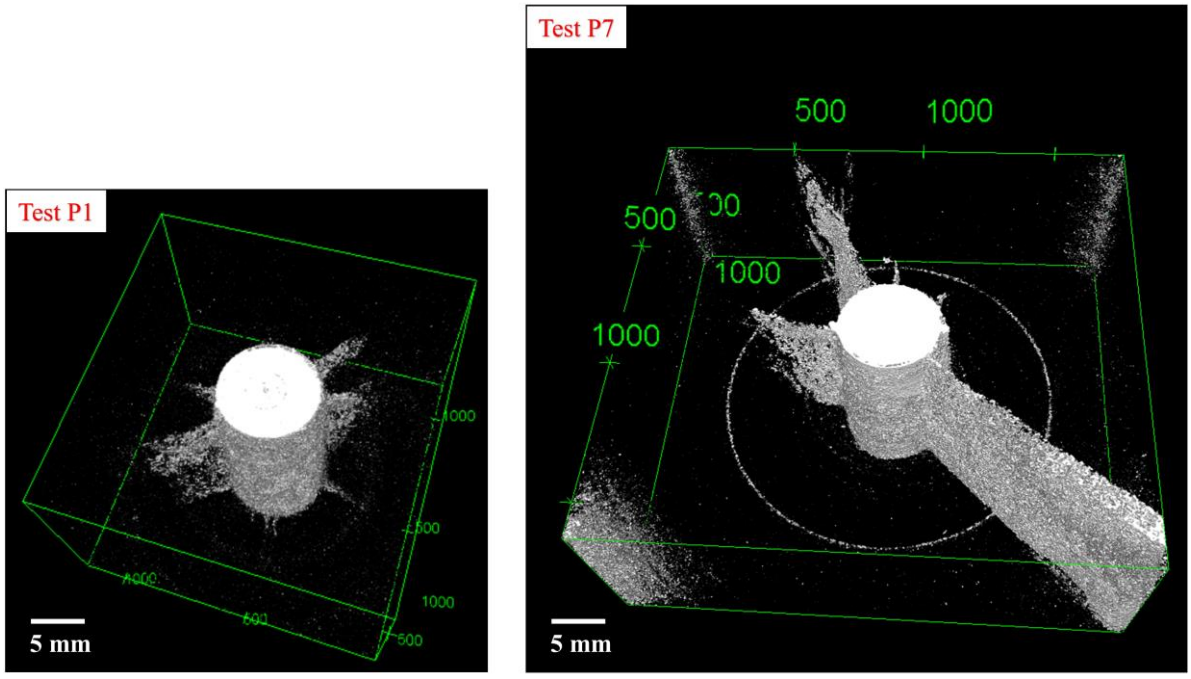

(c) (d)

Fig. 17. Effect of flow rate: (a) pressure vs flow rate curves; (b) increase of the overall permeability; (c), (d) 3D views of the fracturing pattern developed along the injection tube from H = 10 to H = 12 cm for test P1 and P7, respectively.

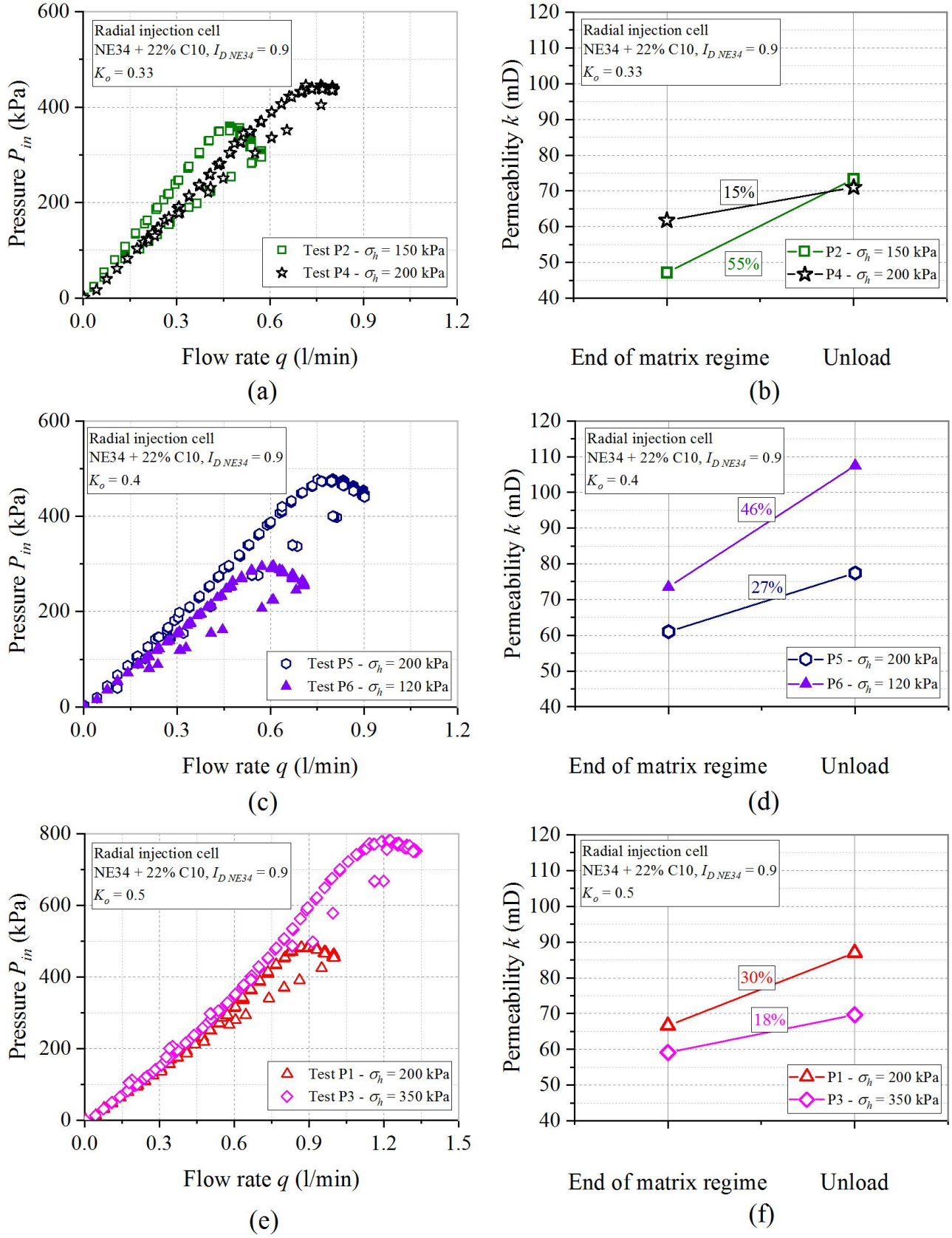

Fig. 18. Effect of confining pressure on the pressure vs flow rate curves and the increase of the overall permeability in the different cases of K_0: (a), (b) K_0 = 0.33; (c), (d) K_0 = 0.4; (e), (f) K_0 = 0.5.

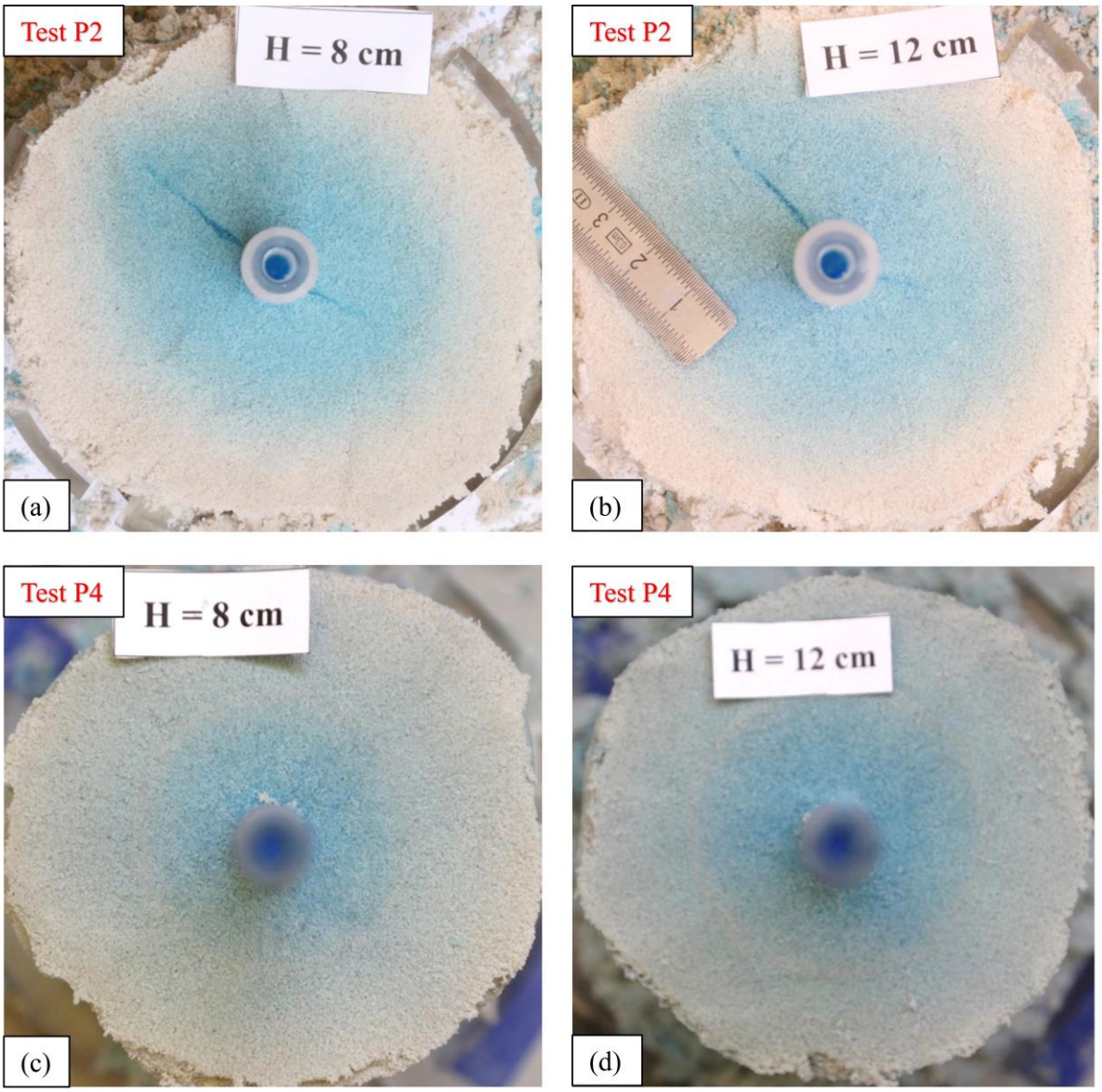

Fig. 19. Photos of the horizontal cross-sections corresponding to different depths of excavation in the case of K_0 = 0.33 : (a), (b) test P2; (c), (d) test P4.

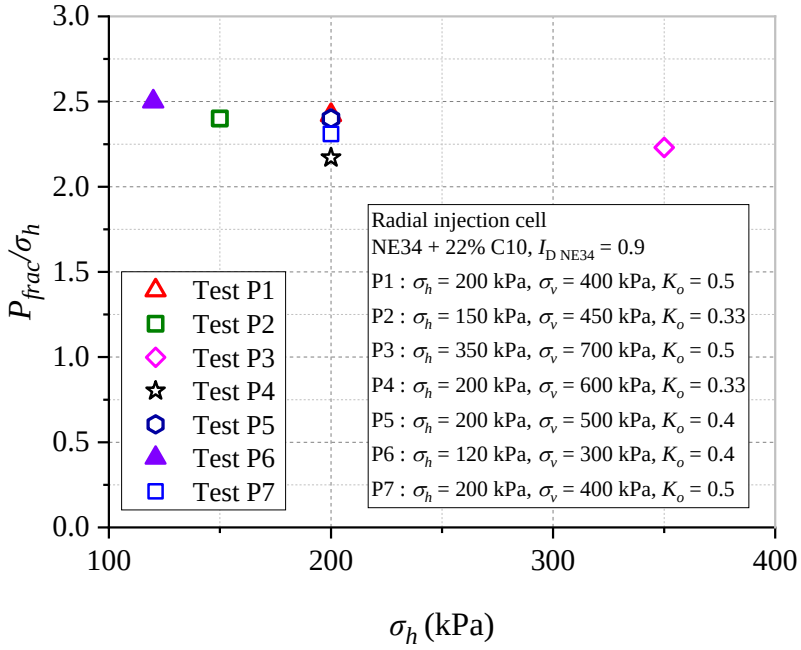

Fig. 20. Effect of confining pressure on the normalized fracturing pressure (P_{frac}/σ_h).

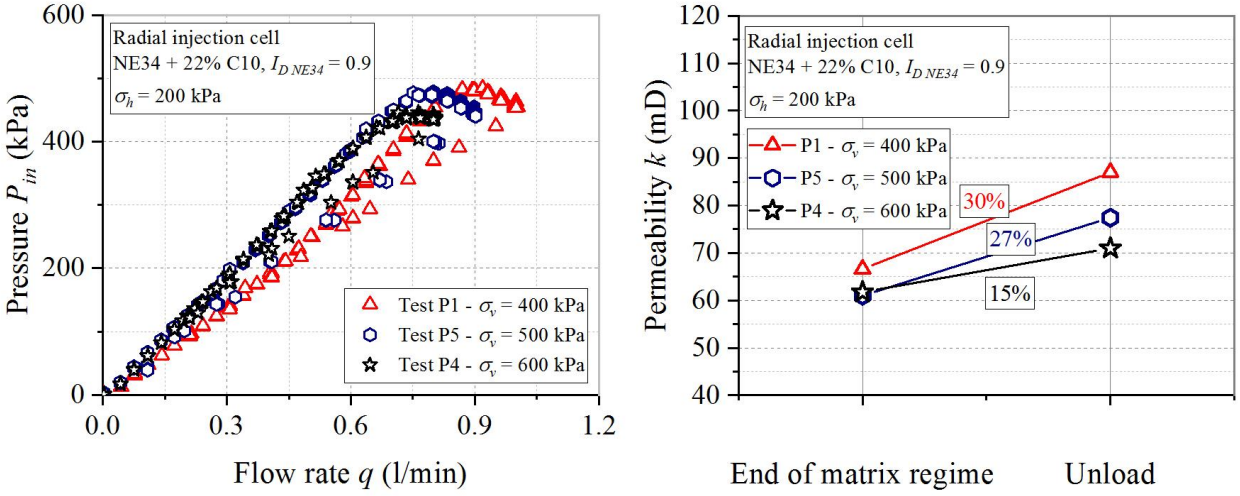

(a) (b)

Fig. 21. Effect of the stress ratio coefficient K_0 on: (a) the pressure vs flow rate curves and (b) the increase of the overall permeability in the different cases.

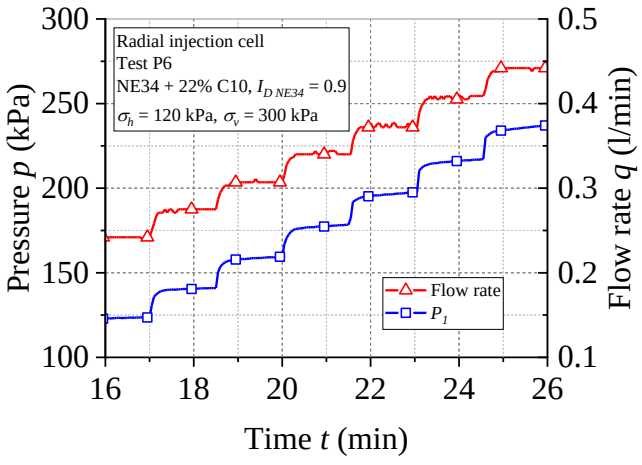

(a)

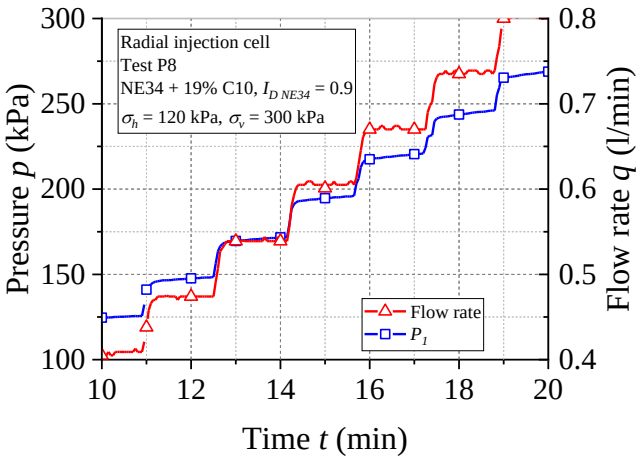

(b)

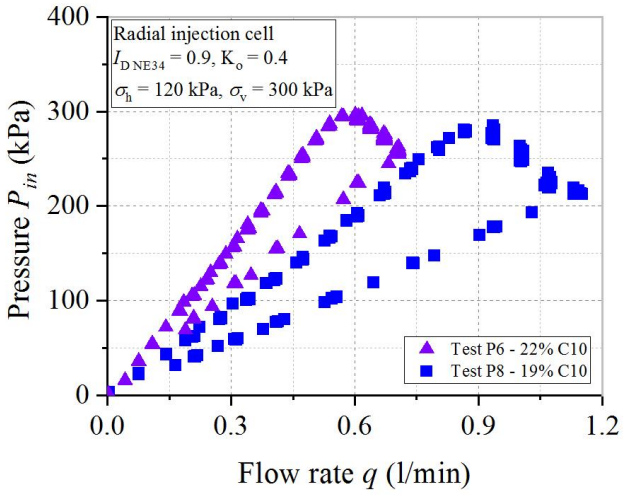

(c)

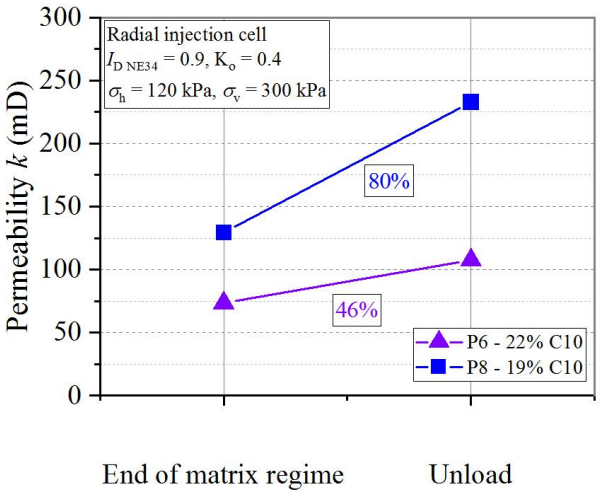

(d)

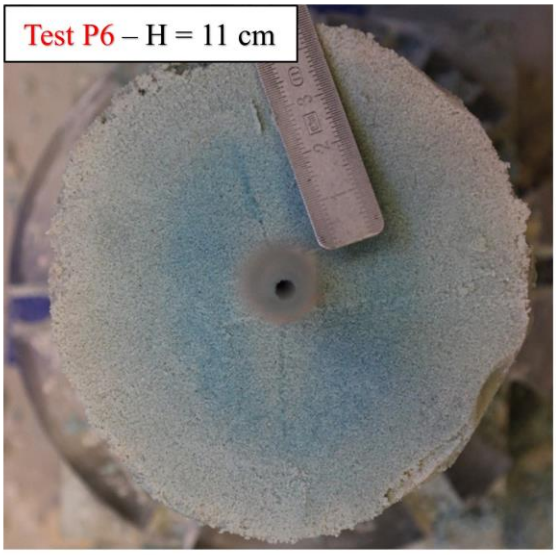

(e)

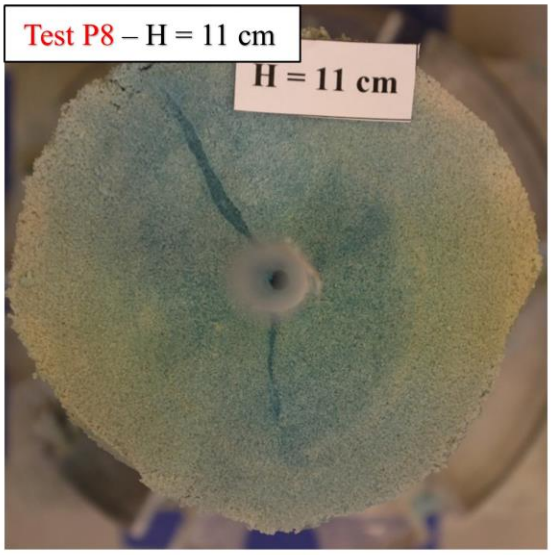

(f)

Fig. 22. Effect of the initial permeability: (a), (b) the pressure – flow rate – time curves during matrix regime of the tests P6 and P8, respectively; (c) the pressure vs flow rate curves; (d) the increase of the overall permeability after fracturing; (e) and (f) typical horizontal cross-sections at H = 11 cm of the tests P6 and P8, respectively.

673

Material	D_{50} (μm)	C_u	e_{min}	e_{max}	Angularity	ρ_s (g/cm^3)
Fontainebleau NE34 sand (after Feia, 2015)	210	1.5	0.55	0.88	Sub-rounded	2.65
C10 silica particles	20	11	-	-	-	2.65

674 **Table 1:** Characteristics of the tested materials

	Colloidal	Accelerator	Mixture
Color	Translucent white	Translucent	Translucent white
Viscosity (mPa.s)	10	1	5
Density (kg/l)	1.3	1.07	1.25
pH	9.5 to 9.8	7	~9 (depend on the dosage)
SiO_2 concentration	40 ± 1	-	-

675 **Table 2:** MasterRoc MP320: Data of BASF Construction Chemical Company

676

Section	Heigh (H)	Materials	Total mass (m)	$I_{D\ NE34}$	Porosity (n)	Dry density (ρ_d)
	cm	-	g	-	(%)	g/cm^3
Upper and lower layers of low permeability	2	NE34 + 32% C10	322	0.6	22	2.08
Injection zone	16	NE34 + 22% C10	2082	0.9	23	2.04

677 **Table 3:** Characteristics of the reference specimen

678

679

680

681

Test condition			Injection zone		Density index of the sand matrix	Fluid injection	
σ_h (kPa)	σ_v (kPa)	K_0	Materials	k (mD)	$I_{D\ NE34}$	Type	μ (cP)
200	400	0.5	NE34 + 22% C10	≈ 80	0.90	Clean water	1

Table 4: Characteristics of the reference test

Test	Parameters	Materials		Fluid		Stress conditions			Density index of the matrix $I_{D\ NE34}$	Number of steps of flow rate increase in the fracturing regime
		% C10	k (mD)	μ (cP)	% fine	σ_h (kPa)	σ_v (kPa)	K_0		
P1	Stress conditions	22	≈ 80	1	0	200	400	0.50	0.90	4
P2		22	≈ 80	1	0	150	450	0.33	0.90	4
P3		22	≈ 80	1	0	350	700	0.50	0.90	4
P4		22	≈ 80	1	0	200	600	0.33	0.90	4
P5		22	≈ 80	1	0	200	500	0.40	0.90	4
P6		22	≈ 80	1	0	120	300	0.40	0.90	4
P7	Flow rate	22	≈ 80	1	0	200	400	0.50	0.90	6
P8	Permeability	19	≈ 150	1	0	120	300	0.40	0.90	4

Table 5: Characteristics of the parametric tests